mathematics

MDPI

Article

Centralized Multi-Objective UAV–UGV Task Allocation for Disaster Relief Material Distribution with Mobile UAV Bases

Yupeng Zhang [1], Shaoxun Liu [1] and Chengxin Wen [2,*]

[1] Endogenous Security Research Center, Purple Mountain Laboratories, Nanjing 211111, China; zhangyupeng@pmlabs.com.cn (Y.Z.); liushaoxun@pmlabs.com.cn (S.L.)
[2] Beijing Institute of Astronautical Systems Engineering, Beijing 100076, China
* Correspondence: chengxinwenbit@gmail.com

Abstract

Coordinating unmanned aerial vehicles (UAVs) and unmanned ground vehicles (UGVs) for post-disaster emergency material distribution requires joint decisions on task allocation, routing, delivery quantities, and rendezvous scheduling. Mobile UGV bases and split deliveries increase operational flexibility but introduce strong dependencies between aerial and ground operations. This paper investigates a centralized multi-objective multi-robot task allocation problem with static, known demands, in which UGVs transport supplies and support UAV launch, recovery, and battery replacement. A three-objective model is formulated to minimize weighted demand completion time, operating cost, and maximum normalized workload, subject to accessibility, payload, inventory, energy, and synchronization constraints. To solve the resulting constrained combinatorial optimization problem, we propose HV-ADEA, a hypervolume-guided adaptive evolutionary algorithm. A hybrid representation jointly encodes UGV stop sequences, UAV–interval task assignments, and split delivery quantities, while a synchronized decoder derives execution times and evaluates feasibility. A bounded iterative repair mechanism addresses coupled constraint violations. Domain-specific variation operators perform joint mobile base–sortie adjustment, aerial–ground quantity transfer, delivery splitting and merging, and synchronization bottleneck reduction to explore alternative allocation and routing plans. An experimental protocol is established using six test configurations of increasing scale and five baseline algorithms: NSGA-II, CCMO, BiCo, EMCMO, and C3M. The test results show that the algorithm we propose is competitive in most of the test cases.

Keywords: multi-objective optimization; multi-robot task allocation; UAV–UGV cooperation; disaster rescue

MSC: 90C9

Check for updates

Academic Editors: Qiang Yang and Weiwei Qian

Received: 14 September 2026
Revised: 14 October 2026
Accepted: 22 October 2026
Published: 29 October 2026

Copyright: © 2026 by the authors. Licensee MDPI, Basel, Switzerland. This article is an open access article distributed under the terms and conditions of the Creative Commons Attribution (CC BY) license.

1. Introduction

Natural disasters frequently damage road networks, isolate affected communities, and create rapidly changing demands for emergency supplies. In such environments, UAVs can provide rapid access to areas that are difficult or impossible to reach by conventional ground vehicles [1]. However, UAVs are limited by payload capacity [2], battery endurance [3], flight range [4], and weather conditions [5]. UGVs, in contrast, generally have larger payload capacities and longer operating durations, but their mobility is strongly restricted by damaged roads, obstacles, and terrain conditions [6]. A heteroge-

neous UAV–UGV team can combine the complementary capabilities of both platforms and provide a more flexible solution for post-disaster material distribution.

The coordination of UAVs and UGVs gives rise to a heterogeneous multi-robot task allocation (MRTA) problem. Specifically, the system must determine which robot should be assigned to each demand point, the amount of material to be delivered, the sequence in which tasks should be executed, and whether UAVs and UGVs should jointly execute a mission [7]. For instance, a UGV may transport a relatively large quantity of supplies to a temporary staging area, followed by UAVs delivering smaller packages to isolated demand points. Alternatively, a UAV may perform reconnaissance while a UGV handles material transportation. These decisions are tightly coupled with route planning, vehicle capacity, energy consumption, task priorities, and mission completion time. Consequently, the problem cannot be adequately formulated as a simple one-to-one assignment problem [8].

Existing studies have investigated various MRTA formulations by considering robot states, task feasibility, objective functions, and dynamic task information. Recent studies have further incorporated heterogeneous robot capabilities, task decomposition, recharging requirements, and online plan repair [9]. In UAV-based emergency logistics, multi-objective optimization models have also been developed to simultaneously minimize total flight distance and workload imbalance subject to payload and route length constraints. However, a substantial portion of the existing literature focuses on homogeneous UAV fleets or single-platform systems [10]. Other studies simplify the operational environment by assuming a single depot, a single delivery trip, static demands, or non-splittable tasks. While these assumptions facilitate model formulation and computational analysis, they limit the applicability of existing approaches to heterogeneous aerial–ground cooperation in realistic disaster response scenarios.

The UAV–UGV setting presents several challenges that arise from the differences in mobility, resource constraints, and operational roles between the two robot types [11,12]. The accessibility of a demand point, for example, is determined not only by the disaster environment but also by the capabilities of the assigned robot. Some locations may be inaccessible to UGVs because of damaged or blocked roads while remaining reachable by UAVs. In contrast, locations with large material requirements may be better served by UGVs because of their higher payload capacity [10,12]. The resource constraints of the two platforms also differ substantially. UAV operations are primarily limited by payload capacity, battery energy, and flight range, whereas UGV operations depend more heavily on road connectivity, travel time, terrain conditions, and ground mobility. In addition, certain missions cannot be completed efficiently by a single robot and therefore require explicit cooperation between UAVs and UGVs, such as UAV deployment from a mobile UGV platform, material transfer between robots, or the sequential execution of reconnaissance and delivery tasks. These operational conditions may also change during a mission as new demand points emerge, road conditions are restored, or robots become unavailable [10,11].

The above factors result in inherent trade-offs among the optimization objectives. Minimizing the total travel distance, for instance, may lead to an uneven distribution of tasks and impose excessive workloads on a limited number of robots [13]. Conversely, achieving a more balanced workload may require additional travel and consequently increase response time or energy consumption. Similarly, giving priority to high-risk or time-critical demand points may result in longer routes and greater resource expenditure. These trade-offs make it difficult to characterize the overall mission objective using a single fixed preference [14]. A multi-objective formulation is therefore adopted to preserve the competing characteristics of the problem rather than combining them into a weighted objective with predetermined coefficients. A multi-objective evolutionary algorithm (MOEA) can subsequently obtain a set of non-dominated allocation and routing solutions, from which an appropriate plan can

be selected according to the operational requirements and the prevailing trade-offs among service effectiveness, response time, energy consumption, operational risk, and workload balance [15].

This paper investigates a multi-objective MRTA problem for heterogeneous UAV–UGV teams in post-disaster emergency material distribution. The proposed model jointly considers robot–task compatibility, heterogeneous payload and endurance constraints, the accessibility of damaged roads, material demand, task priority, route feasibility, and inter-robot cooperation. The objectives are designed to minimize emergency service loss, operational cost and risk, and workload imbalance across the heterogeneous fleet. To solve the resulting constrained combinatorial optimization problem, we develop a hypervolume-guided adaptive evolutionary algorithm (HV-ADEA), an MOEA that combines a hybrid encoding of UGV stop sequences, UAV–interval task assignments, and split delivery quantities, a bounded iterative repair mechanism for route–sortie consistency, payload and energy limits, demand balance, and inventory constraints, and domain-specific variation operators for joint mobile base–sortie adjustment, aerial–ground quantity transfer, delivery splitting and merging, and synchronization bottleneck reduction to improve the search for feasible Pareto-optimal solutions. The main contributions of this work are summarized as follows:

- A heterogeneous UAV–UGV MRTA model is formulated for post-disaster material distribution, integrating task allocation, material delivery, route planning, and inter-robot cooperation.
- A multi-objective optimization framework is developed to capture the trade-offs among emergency service effectiveness, response efficiency, operational risk, and workload fairness.
- A problem-specific MOEA is proposed with an allocation–routing representation and feasibility-preserving repair operators for handling heterogeneous capacity, battery, accessibility, and cooperation constraints.
- Extensive experiments are conducted under different disaster scales, demand patterns, road disruption levels, and fleet compositions. The proposed method is evaluated using Pareto front quality indicators and application-oriented metrics, including hypervolume, inverted generational distance (IGD), feasible solution ratio, unmet demand, response time, energy consumption, and workload imbalance.

2. Related Work

2.1. Multi-Robot Task Allocation

MRTA determines how a set of tasks should be assigned to a team of robots while satisfying robot capabilities, task feasibility, and mission-level objectives. Recent general formulations have emphasized that MRTA is not limited to a binary assignment relationship. Robot states, task requirements, environmental conditions, feasibility constraints, and objective functions may all be incorporated into the problem formulation. Existing solution approaches include mathematical programming, market-based mechanisms, heuristic methods, and distributed negotiation strategies [16].

Task scheduling is often considered together with task allocation because the quality of an assignment depends on the order and timing of task execution. A survey of task allocation and scheduling in robotic network systems categorized existing studies according to system architecture, application scenario, algorithmic method, and optimization parameter. The survey highlighted completion time, delay, energy consumption, resource utilization, and the number of completed tasks as common performance measures [17]. However, many general MRTA studies use abstract robot–task compatibility models and do not explicitly represent the physical interaction between aerial and ground vehicles.

For heterogeneous robot teams, allocation feasibility depends on platform-specific capabilities. A robot may be suitable for a task because of its payload, sensing ability, mobility, energy level, or communication capability. This makes heterogeneous MRTA substantially different from homogeneous assignment, where robots can often be treated as interchangeable. In addition, some tasks may require multiple robots, task fragmentation, task relaying, or intermediate recharging. Calvo and Capitán formulated a heterogeneous MRTA problem for long-endurance missions and considered recharging, task fragmentation, task relaying, coalition tasks, and online plan repair [18]. Their work demonstrates the importance of integrating robot endurance and task execution structure into the allocation model. Nevertheless, the framework is mainly formulated as a general heterogeneous mission-planning problem and does not specifically investigate UAVs operating from mobile UGV bases.

2.2. UAV–UGV Heterogeneous Cooperation

UAV–UGV systems combine the complementary mobility and operational capabilities of aerial and ground platforms. UAVs can rapidly reach locations that are difficult or inaccessible for ground vehicles, while UGVs typically provide higher payload capacity, longer endurance, and greater flexibility for carrying supplies or supporting UAV operations [19,20]. This complementarity has led to increasing research on aerial–ground cooperation in disaster response, medical rescue, surveillance, inspection, and logistics. Rather than treating UAVs and UGVs as independent platforms, these studies investigate how their different capabilities can be coordinated to improve mission efficiency under constrained operating conditions [19,20].

A number of studies have addressed joint task allocation and trajectory planning for UAV–UGV teams. Chen et al. [21] investigated UAV–UGV cooperation for medical rescue in post-disaster environments. Their approach combines genetic algorithm-based task allocation with informed RRT* for collision-free trajectory generation and CMA-ES for task sequencing and path optimization. The results show that coordinated aerial–ground operations can reduce mission completion time and travel distance compared with independent allocation strategies [21]. Similar studies have considered the coordination of heterogeneous robots under constraints related to payload, operating range, task deadlines, and environmental accessibility [10,19]. These works demonstrate the advantages of joint UAV–UGV planning, but the allocation and routing decisions are often handled sequentially or under relatively simplified task structures.

A more closely related research direction uses UGVs as mobile support platforms for UAV operations. In such systems, a UGV can transport one or more UAVs, provide launch and landing locations, extend the effective operating range of UAVs, or support UAV deployment and recovery [15,20]. The introduction of a mobile base changes the task allocation problem substantially. The feasibility of a UAV task is no longer determined solely by the UAV's payload and flight range; it also depends on the location and route of the supporting UGV, the timing of UAV deployment and recovery, and the synchronization between the two platforms. Consequently, ground routing and UAV sortie planning become interdependent with task assignment, creating a coupled decision problem rather than a conventional independent task allocation process.

This coupling has been investigated in several truck–drone and UGV–UAV routing studies, particularly for delivery and emergency logistics. Existing approaches have considered decisions on aspects such as UAV launch and recovery locations, rendezvous between aerial and ground vehicles, and the joint optimization of ground routes and UAV sorties [14,20]. These studies show that a mobile ground platform can substantially enlarge the set of locations that can be served by UAVs. At the same time, an inappropriate ground route may increase synchronization requirements, reduce the number of feasible UAV sorties,

or cause additional energy consumption. Thus, the mobile base decision directly affects both task feasibility and the overall quality of the allocation plan.

2.3. Integrated Task Allocation and Planning

Recent research has increasingly considered task allocation and motion planning simultaneously. Luo and Liu proposed a search-based method for simultaneous task allocation and planning under hierarchical temporal logic specifications [22]. Their work models task dependencies and temporal requirements and provides theoretical analysis of completeness and optimality. Similarly, Liu et al. formulated multi-robot task allocation and coordination under signal temporal logic specifications, using candidate paths and mixed-integer linear programming to satisfy complex temporal requirements [23].

Graph-based learning methods have also been applied to simultaneous allocation and scheduling. Altundas et al. proposed a heterogeneous graph Transformer for mobile multi-robot task allocation and scheduling under temporal constraints [24]. Their method represents agent capabilities, travel times, and temporal constraints in a graph and learns a one-shot allocation and scheduling policy. These approaches are effective for representing dependencies and temporal feasibility, but they generally do not model UGVs as mobile UAV bases or allow a task to be divided between aerial and ground robots.

A related line of research considers dynamic or uncertain mission conditions. In wildfire response, drone task planning has been coupled with fire spread prediction and chance-constrained robust optimization [25]. In long-endurance heterogeneous missions, online repair and replanning are used to respond to unexpected events [18]. Such methods are valuable for real-time operation, but the present study focuses on an offline centralized planning problem in which the task set and environment are known before execution. This setting allows the planner to optimize the complete allocation, deployment, routing, and task-splitting decisions jointly. Table 1 summarizes the modeling features considered in representative rescue-related MRTA studies and highlights the combination of centralized planning, UAV–UGV cooperation, mobile UAV bases, task splitting, joint allocation–routing, and multi-objective optimization addressed in this study.

Table 1. Comparison of factors considered in rescue-related MRTA studies.

Reference	Centralized	UAV–UGV	Mobile UAV Base	Task Splitting	Joint Allocation–Routing	Payload/ Endurance	Temporal Constraints	Dynamic Replanning	Multi-Objective
Aziz et al. [16]	Partial	Partial	–	Partial	Partial	Partial	Partial	Partial	Partial
Alirezazadeh and Alexandre [17]	Partial	Partial	–	–	Partial	✓	Partial	Partial	Partial
Calvo and Capitán [18]	✓	Heterogeneous robots	–	✓	✓	✓	Partial	✓	–
Chen et al. [21]	✓	✓	Unclear	Unclear	Partial	Partial	–	–	–
Luo and Liu [22]	✓	–	–	–	✓	Partial	✓	–	–
Liu et al. [23]	✓	–	–	–	✓	Partial	✓	–	–
Altundas et al. [24]	✓	✓	–	–	✓	✓	✓	–	–
Pan et al. [25]	✓	UAV swarm	–	Partial	✓	✓	✓	Partial	–
Shang et al. [14]	✓	Limited UAV heterogeneity	–	–	✓	✓	–	–	✓
This study	✓	✓	✓	✓	✓	✓	✓	–	✓

In summary, existing research has addressed general MRTA, heterogeneous robot capabilities, UAV–UGV cooperation, temporal task planning, and multi-objective UAV logistics. However, the combination of the following features has received limited attention: centralized joint planning of a heterogeneous UAV–UGV team, UGVs serving as mobile UAV bases, divisible delivery tasks, and Pareto optimization of allocation and routing decisions. This study addresses this combination by developing a centralized multi-objective MRTA model for post-disaster material distribution. The model jointly determines task assignment, task splitting, UAV deployment from UGVs, ground and aerial routes, and mission-level objective trade-offs.

3. System Model and Problem Formulation

3.1. System Description and Assumptions

We consider post-disaster emergency material distribution using a heterogeneous team of UGVs and UAVs. UGVs transport relief supplies, directly serve ground-accessible demand points, and act as mobile bases for their assigned UAVs. UAVs carry smaller shipments from their supporting UGVs to demand points and subsequently rendezvous with the same UGVs. The planner jointly determines ground routes, UAV sorties, delivery quantities, and synchronized execution times. The following assumptions define the scope of the model:

1. Planning is centralized and static. Demands, robot capabilities, road accessibility, and travel times are known before execution. Online replanning is outside the scope of this study; nevertheless, the resulting offline solution can serve as the initial nominal plan for a rolling/receding-horizon implementation in which already executed decisions are fixed and the remaining allocation, routing, and air–ground synchronization decisions are re-optimized from the current system state when updated demand, travel time, or robot availability information becomes available [18].
2. A single divisible commodity is considered. A demand may be fulfilled by multiple UGVs, multiple UAV sorties, or a combination of both platforms. Task splitting refers to splitting delivery quantities.
3. Each UAV is assigned to one UGV throughout the mission. Each sortie serves one demand point and returns to its supporting UGV, potentially at a location different from the launch location.
4. UGV routes are represented by a finite sequence of stopping stages. Each UAV performs at most one sortie between consecutive stages, and all dispatched UAVs must be recovered before the next stage begins. Repeated stops are permitted. Sorties spanning multiple ground route intervals are excluded from this formulation.
5. All supplies are loaded initially. No material replenishment, including intermediate visits to the depot, occurs during the mission. UAV batteries can be exchanged after recovery, subject to a finite usable energy budget carried by the supporting UGV. Battery inventory is represented by an aggregate energy budget rather than individual battery pack scheduling.
6. Ground delivery precedes launch preparation at each stage. Launch preparation and recovery can be performed in parallel for different UAVs, assuming sufficient handling resources. An early-arriving UAV can land safely and wait at the rendezvous location with negligible waiting energy. Recovery and battery exchange begin only after both vehicles are present.

Ground and aerial travel parameters are obtained from precomputed feasible paths. Damaged roads and no-fly regions are therefore represented through admissible connections and their associated travel parameters. The model optimizes routes over these

connections; continuous trajectory generation and inter-robot collision avoidance are not decision layers in this model.

3.2. Sets, Parameters, and Decision Variables

Let $\mathcal{G}$ denote the UGV set and $\mathcal{A}_g$ the UAVs assigned to UGV g, with disjoint UAV sets across UGVs. Let $\mathcal{N}$ be the demand set, and let $\mathcal{V}$ contain the depot 0, candidate rendezvous sites, and ground service demand nodes. Define $\mathcal{N}^G = \mathcal{N} \cap \mathcal{V}$, where the depot is not a demand node. For UGV g, $\mathcal{E}_g \subseteq \mathcal{V} \times \mathcal{V}$ contains its admissible ground connections. Self-loops (i, i) are permitted with zero travel time and zero travel cost. Unreachable nodes cannot be reached by a route from the depot.

The stopping stage sets are

$$\mathcal{K} = \{0, \dots, K\}, \qquad \mathcal{K}^- = \{0, \dots, K-1\}. \tag{1}$$

Here, K is a prescribed upper bound on the number of operating intervals. Unused intervals may be padded by repeated depot stops. Consequently, the formulation is exact for the stated stage-limited operating policy, and the selected K must be sufficiently large for the intended instances.

For compact notation, a candidate sortie is denoted by $s = (i, h, j)$, with launch node i, demand point h, and recovery node j. Let $\mathcal{S}_{ga}$ contain admissible sorties for UAV $a \in \mathcal{A}_g$, requiring $(i, j) \in \mathcal{E}_g$ and feasible aerial connections. Define $\mathcal{S}_{ga}(h) = \{(i, h', j) \in \mathcal{S}_{ga} : h' = h\}$. The notation u_{agks} is equivalent to u_{agkihj} in an expanded index representation. The principal parameters used throughout the formulation are summarized in Table 2.

Table 2. Principal model parameters.

Symbol	Definition
$d_h, w_h > 0$	Demand quantity and urgency weight at point h.
Q_g, Q_a	Usable material capacity of UGV g and payload capacity of UAV a.
$B_a, \mathcal{B}_g$	Usable sortie energy and aggregate UAV energy budget on UGV g.
t^G_{gij}, c^G_{gij}	Ground travel time and operating cost on connection (i, j).
$t^{\text{out}}_{as}, t^{\text{in}}_{as}$	UAV travel times from launch to demand and from demand to recovery.
s^0_g, ρ_g	Fixed ground service time and service time per delivered unit.
s^0_a, ρ_a	Fixed aerial delivery service time and service time per delivered unit.
ℓ_a, r_a	Launch preparation time and recovery time including battery exchange.
e^0_{as}, κ_{as}	Fixed sortie energy and additional energy per delivered unit.
c^A, c^S_a	Cost per unit UAV energy and fixed cost per sortie.
$\bar{W}_g, \bar{W}_a > 0$	Platform-specific reference active work budgets.
H, M	Planning horizon and sufficiently large time relaxation constant.

All travel, service, energy, and cost coefficients are nonnegative. Capacities Q_g exclude the mass reserved for UAVs, batteries, and equipment. Usable energy parameters incorporate any prescribed safety reserves.

The binary variable p_{gki} selects the stopping node of UGV g at stage k, and z_{gkij} selects its connection between stages k and $k+1$. The binary variable u_{agks} selects sortie s for UAV a in interval k. Continuous variables q^G_{gkh} and q^A_{agks} denote delivered quantities; b_{gkh} indicates a ground service visit. Ground service variables are defined only for $h \in \mathcal{N}^G$ and interpreted as zero otherwise.

The time T_{gk} is the instant at which the UGV is present and all UAVs from the preceding interval have completed recovery. The time D_{gk} denotes departure after ground service and launch preparation. The variable C_h represents full demand completion time, and η bounds the maximum normalized active workload. Auxiliary variables v_{agk}, S^G_{gk}, L_{gk}, E_{agks}, W_g, and W_a are defined below.

3.3. Routing and Mobile Base Constraints

Each UGV occupies exactly one node at every stage and starts and finishes at the depot:

$$\sum_{i \in \mathcal{V}} p_{gki} = 1, \qquad g \in \mathcal{G},\ k \in \mathcal{K}, \tag{2}$$

$$p_{g,0,0} = p_{g,K,0} = 1, \qquad g \in \mathcal{G}. \tag{3}$$

Consecutive stops are connected by admissible ground movements:

$$\sum_{j:(i,j) \in \mathcal{E}_g} z_{gkij} = p_{gki}, \qquad g \in \mathcal{G},\ k \in \mathcal{K}^-,\ i \in \mathcal{V}, \tag{4}$$

$$\sum_{i:(i,j) \in \mathcal{E}_g} z_{gkij} = p_{g,k+1,j}, \qquad g \in \mathcal{G},\ k \in \mathcal{K}^-,\ j \in \mathcal{V}. \tag{5}$$

The stage representation produces a connected route without separate subtour elimination constraints.

UAV sorties must share the launch and recovery stops of their supporting UGV:

$$u_{agks} \le z_{gkij}, \qquad s = (i,h,j) \in \mathcal{S}_{ga}, \tag{6}$$

$$v_{agk} = \sum_{s \in \mathcal{S}_{ga}} u_{agks} \le 1. \tag{7}$$

These constraints apply to every $g \in \mathcal{G}$, $a \in \mathcal{A}_g$, and $k \in \mathcal{K}^-$. Different UAVs may fly concurrently. A sortie with $i \neq j$ enables simultaneous ground movement and aerial delivery, whereas $i = j$ represents launch and recovery at a stationary base.

3.4. Split Deliveries and Resource Feasibility

Every demand must be fully satisfied:

$$\sum_{g \in \mathcal{G}} \sum_{k \in \mathcal{K}^-} q^G_{gkh} + \sum_{g \in \mathcal{G}} \sum_{a \in \mathcal{A}_g} \sum_{k \in \mathcal{K}^-} \sum_{s \in \mathcal{S}_{ga}(h)} q^A_{agks} = d_h, \quad h \in \mathcal{N}. \tag{8}$$

There is no single-visit restriction, allowing a demand to be split across robots and operating intervals. Quantities are linked to selected services:

$$0 \le q^G_{gkh} \le d_h b_{gkh}, \qquad b_{gkh} \le p_{gkh}, \qquad g \in \mathcal{G},\ k \in \mathcal{K}^-,\ h \in \mathcal{N}^G, \tag{9}$$

$$0 \le q^A_{agks} \le \min\{Q_a, d_h\} u_{agks}, \qquad s = (i,h,j) \in \mathcal{S}_{ga}. \tag{10}$$

Equation (10) applies to all valid g, a, k. No positive minimum shipment size is imposed in this continuous-demand model. Selected zero-quantity services are redundant and may be removed without degrading any objective.

Ground deliveries and associated aerial deliveries consume the same initial UGV inventory:

$$\sum_{k \in \mathcal{K}^-} \sum_{h \in \mathcal{N}^G} q^G_{gkh} + \sum_{a \in \mathcal{A}_g} \sum_{k \in \mathcal{K}^-} \sum_{s \in \mathcal{S}_{ga}} q^A_{agks} \le Q_g, \quad g \in \mathcal{G}. \tag{11}$$

Because inventory only decreases, this aggregate constraint also prevents intermediate stock depletion below zero for the prescribed deliveries.

A linear approximation describes sortie energy:

$$E_{agks} = e^0_{as} u_{agks} + \kappa_{as} q^A_{agks}, \tag{12}$$

$$E_{agks} \le B_a u_{agks}, \tag{13}$$

$$\sum_{a \in \mathcal{A}_g} \sum_{k \in \mathcal{K}^-} \sum_{s \in \mathcal{S}_{ga}} E_{agks} \le \mathcal{B}_g, \quad g \in \mathcal{G}. \tag{14}$$

The first two constraints hold for all valid g, a, k, s. The fixed term includes unloaded flight, take-off, landing, and fixed service operations; the quantity-dependent term accounts for payload transport and additional delivery handling. These coefficients must be calibrated to the selected platforms. UGV driving endurance is assumed to be sufficient for routes completed within H; a separate ground energy budget is not imposed in this baseline.

3.5. Ground–Air Synchronization

Ground service duration and parallel launch preparation satisfy

$$S^G_{gk} = \sum_{h \in \mathcal{N}^G} \left(s^0_g b_{gkh} + \rho_g q^G_{gkh} \right), \tag{15}$$

$$L_{gk} \geq \ell_a v_{agk}, \quad a \in \mathcal{A}_g, \tag{16}$$

$$D_{gk} \geq T_{gk} + S^G_{gk} + L_{gk}. \tag{17}$$

These constraints hold for all $g \in \mathcal{G}$, $k \in \mathcal{K}^-$. The ground vehicle must reach its next stop before the next stage starts:

$$T_{g,k+1} \geq D_{gk} + \sum_{(i,j) \in \mathcal{E}_g} t^G_{gij} z_{gkij}. \tag{18}$$

In addition, recovery can finish only after both the ground vehicle and the dispatched UAV are present:

$$T_{g,k+1} \geq D_{gk} + \sum_{(i,j) \in \mathcal{E}_g} t^G_{gij} z_{gkij} + r_a v_{agk}, \tag{19}$$

$$T_{g,k+1} \geq D_{gk} + t^{\text{out}}_{as} + s^0_a + \rho_a q^A_{agks} + t^{\text{in}}_{as} + r_a - M(1 - u_{agks}). \tag{20}$$

Equation (19) holds for every valid g, a, k, and (20) additionally for $s \in \mathcal{S}_{ga}$. For a selected sortie, these inequalities implement

$$T_{g,k+1} \geq \max\{\text{UGV arrival}, \text{UAV arrival}\} + r_a. \tag{21}$$

Thus, recovery time is counted even when the UAV reaches the rendezvous before its supporting UGV. Parallel recovery is assumed across UAVs.

Time bounds are

$$T_{g0} = 0, \qquad 0 \leq T_{gk} \leq H, \qquad g \in \mathcal{G},\ k \in \mathcal{K}, \tag{22}$$

$$0 \leq D_{gk} \leq H, \qquad 0 \leq L_{gk} \leq H, \qquad g \in \mathcal{G},\ k \in \mathcal{K}^-. \tag{23}$$

These conditions also require every UGV and its UAVs to complete the mission at the depot by H.

3.6. Demand Completion Times

Full demand completion occurs after the final shipment has been unloaded. It is represented by

$$C_h \geq T_{gk} + S^G_{gk} - M(1 - b_{gkh}), \qquad h \in \mathcal{N}^G, \tag{24}$$

$$C_h \geq D_{gk} + t^{\text{out}}_{as} + s^0_a + \rho_a q^A_{agks} - M(1 - u_{agks}), \qquad s \in \mathcal{S}_{ga}(h), \tag{25}$$

$$0 \leq C_h \leq H, \qquad h \in \mathcal{N}. \tag{26}$$

The first two inequalities hold over their valid vehicle and interval indices. Since every urgency weight is positive and completion time is minimized, C_h equals the latest selected delivery completion time in an efficient solution after redundant zero-quantity

services are removed. The metric measures full satisfaction rather than the benefit of early partial deliveries.

A safe common relaxation constant for the above time constraints is

$$M = H + \max\left\{0, \max_{g,a,s\in\mathcal{S}_{ga}} \left(t_{as}^{\text{out}} + s_a^0 + t_{as}^{\text{in}} + r_a\right)\right\}, \tag{27}$$

where the inner maximum ranges over valid g, and $a \in \mathcal{A}_g$ and is omitted if there are no candidate sorties. Shipment quantities vanish when the corresponding service is inactive. Tighter constraint-specific constants or solver indicator constraints may be used in implementation.

3.7. Multi-Objective Formulation

Three objectives capture service timeliness, operating cost, and peak normalized active workload.

3.7.1. Urgency-Weighted Completion Time

The first objective is

$$\min f_1 = \frac{\sum_{h\in\mathcal{N}} w_h C_h}{\sum_{h\in\mathcal{N}} w_h}. \tag{28}$$

A larger w_h places greater emphasis on earlier full satisfaction of demand h.

3.7.2. Total Operating Cost

The second objective is

$$\begin{aligned}\min f_2 = &\sum_{g\in\mathcal{G}} \sum_{k\in\mathcal{K}^-} \sum_{(i,j)\in\mathcal{E}_g} c_{gij}^G z_{gkij} \\ &+ \sum_{g\in\mathcal{G}} \sum_{a\in\mathcal{A}_g} \sum_{k\in\mathcal{K}^-} \sum_{s\in\mathcal{S}_{ga}} \left(c^A E_{agks} + c_a^S u_{agks}\right).\end{aligned} \tag{29}$$

All terms are expressed in a common monetary unit. Fixed sortie costs represent launch, battery exchange, and maintenance overhead and discourage unnecessary shipment fragmentation.

3.7.3. Maximum Normalized Active Workload

Ground and aerial active workloads are defined as

$$W_g = \sum_{k\in\mathcal{K}^-} \sum_{(i,j)\in\mathcal{E}_g} t_{gij}^G z_{gkij} + \sum_{k\in\mathcal{K}^-} S_{gk}^G, \tag{30}$$

$$W_a = \sum_{k\in\mathcal{K}^-} \sum_{s\in\mathcal{S}_{ga}} \left[\left(t_{as}^{\text{out}} + t_{as}^{\text{in}} + s_a^0 + \ell_a + r_a\right) u_{agks} + \rho_a q_{agks}^A\right], \quad a \in \mathcal{A}_g. \tag{31}$$

These measures exclude idle waiting. Ground workload also excludes UAV handling, which is assigned to the aerial workload measure. They therefore measure the specified active operations rather than total elapsed mission time. The third objective and its epigraph constraints are

$$\min f_3 = \eta, \tag{32}$$

$$W_g \le \eta \bar{W}_g, \quad g \in \mathcal{G}, \tag{33}$$

$$W_a \le \eta \bar{W}_a, \quad g \in \mathcal{G},\ a \in \mathcal{A}_g. \tag{34}$$

At efficiency, η equals the largest platform-normalized workload. This objective reduces peak utilization; it does not directly minimize workload variance or demand-side inequity. Reference budgets are fixed input parameters, not hard limits, so η may exceed one. Hard operational limits, if required, can be added separately as $W_r \le \bar{W}_r$.

3.7.4. Complete Optimization Problem

Let $\boldsymbol{x}$ collect all decision and auxiliary variables. The centralized multi-objective problem is

$$\begin{aligned} \min_{\boldsymbol{x}} \quad & \boldsymbol{F}(\boldsymbol{x}) = (f_1, f_2, f_3), \\ \text{subject to} \quad & (2)\text{–}(26), \\ & (30),\ (31), \\ & (33),\ (34), \\ & p_{gki}, z_{gkij}, u_{agks}, b_{gkh}, v_{agk} \in \{0,1\}, \\ & q^G_{gkh}, q^A_{agks}, E_{agks}, S^G_{gk}, W_g, W_a, \eta \geq 0. \end{aligned} \tag{35}$$

All variable domains apply only to their defined indices; time-variable domains are given explicitly above. With fixed path parameters and the linear energy approximation, this is a multi-objective mixed-integer linear program under the stated operational assumptions.

A feasible solution dominates another if it is no worse in all three objectives and strictly better in at least one. The goal is to approximate the set of non-dominated feasible plans using a multi-objective evolutionary algorithm. Small instances may be evaluated against mathematical programming solutions, for example, through an ϵ constraint procedure.

The key couplings can be described as follows: split shipment quantities affect UAV energy requirements, UGV stops determine feasible UAV launch and recovery locations, and rendezvous synchronization propagates delays to subsequent deliveries. For evolutionary optimization, a solution can therefore encode UGV stopping sequences, UAV sorties, and shipment quantities. Given these choices, the earliest feasible schedule is computed recursively from the synchronization constraints, avoiding the need to evolve time variables independently.

4. A Hypervolume-Guided Adaptive Decomposition Evolutionary Algorithm

The model in Section 3 is a constrained multi-objective mixed-integer optimization problem. Directly solving it with an exact method is impractical for large instances because the decisions on UGV routes, UAV sorties, divisible delivery quantities, inventory, energy, and air–ground synchronization are strongly coupled. We therefore develop a hypervolume-guided adaptive decomposition evolutionary algorithm, abbreviated as HV-ADEA. The algorithm combines decomposition-based mating and replacement with a hypervolume (HV)-based external archive. In addition, the decomposition directions are periodically adjusted according to the HV gains produced by feasible offspring.

4.1. Overall Framework

Let the three minimization objectives be written as

$$\mathbf{f}(x) = \big(f_1(x), f_2(x), f_3(x)\big), \qquad x \in \Omega, \tag{36}$$

where Ω is the feasible solution set defined by the constraints in Section 3. HV-ADEA maintains two complementary populations:

- A decomposition population $D = \{x^1, \ldots, x^{N_D}\}$, in which each solution is associated with one decomposition direction and is used to maintain search diversity;
- An external archive A, which stores feasible non-dominated solutions and uses HV contribution for environmental selection.

The decomposition population provides directional search pressure, whereas the archive preserves solutions that cover a large region of the objective space. These two

roles are deliberately separated: a solution can remain useful for a decomposition subproblem even when it has a small immediate HV contribution, while infeasible solutions may temporarily remain in D to guide constraint repair but are never inserted into the feasible archive.

4.2. Solution Representation and Decoding

A solution is represented by three coupled components,

$$x = (R, S, Q), \tag{37}$$

where R denotes the stop sequence of each UGV, S specifies the demand point served by each UAV–interval pair, and Q contains direct and aerial delivery quantities. Figure 1 illustrates the correspondence between these components, the resulting delivery plan, and the decoding procedure.

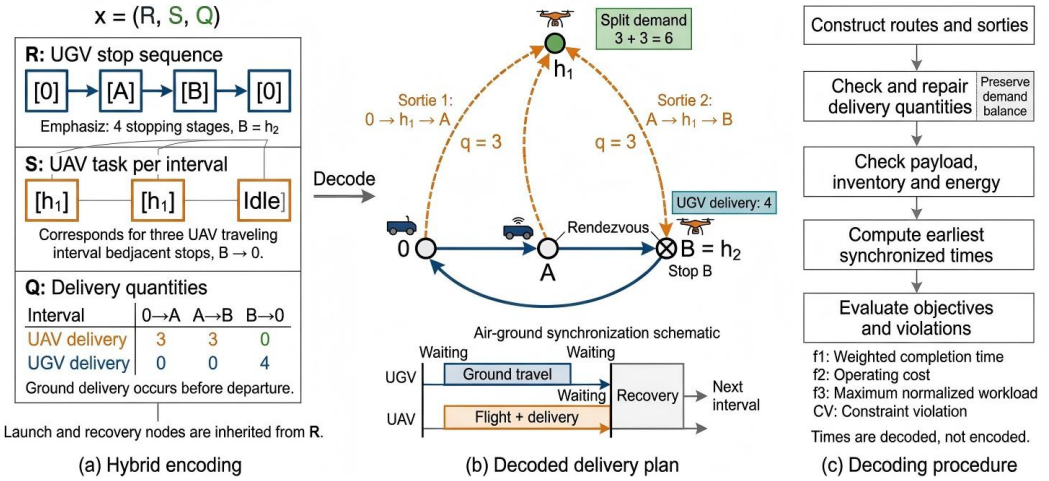


Figure 1. Solution representation and decoding: (**a**) Hybrid encoding of UGV stop sequences, UAV assignments, and delivery quantities. (**b**) The corresponding delivery plan. (**c**) Decoding procedure for constructing the delivery plan.

As shown in Figure 1a, a UGV route is represented as a sequence of stopping nodes that starts and ends at the depot. Repeated consecutive nodes are allowed and represent waiting at the same mobile base. Each interval corresponds to two consecutive stops. For a UGV g moving from node i to node j during interval k, a gene $S_{agk} = h$ means that UAV a assigned to g takes off from i, serves demand point h, and is recovered at j. An idle gene, denoted by $\emptyset$, indicates that the UAV remains onboard and performs no delivery during that interval. Consequently, the take-off and recovery nodes are inherited from the UGV route rather than encoded independently. This representation automatically preserves the relationship between a UAV sortie and its mobile UGV base.

The example in Figure 1a contains one UGV G_1 and its associated UAV U_1. Their route and assignment sequences are

$$R_1 = (0, A, B, 0), \qquad S_{U_1} = (h_1, h_1, \emptyset). \tag{38}$$

The four UGV stops define three intervals, corresponding to $0 \to A$, $A \to B$, and $B \to 0$. The aerial delivery quantities over these intervals are $(3, 3, 0)$, while the direct delivery quantities are $(0, 0, 4)$. Direct ground delivery occurs at the current stop before departure; therefore, the four units associated with the final interval are delivered at $B = h_2$ rather than at the depot.

Figure 1b shows how these genes define the delivery plan. During the first interval, G_1 travels from 0 to A, while U_1 follows $0 \to h_1 \to A$ and delivers three units to h_1. After recovery

at A, the UAV executes a second sortie, $A \to h_1 \to B$, delivering another three units while the UGV moves to B. The six-unit demand at h_1 is thus split across two successive sorties. After UAV recovery at B, the UGV directly delivers four units to h_2 and returns to the depot with the UAV onboard. All ten units are initially carried by G_1. This example illustrates how R, S, and Q jointly describe mobile base operation and demand splitting.

The decoding procedure follows the five stages shown in Figure 1c: 1. route and sortie association; 2. delivery quantity allocation; 3. inventory and energy checking; 4. air–ground time propagation; 5. objective evaluation. The decoder first constructs the ground routes and associated UAV sorties from R and S. It then checks the quantities in Q and, where necessary, repairs their allocation while preserving demand balance. Payload limits, UGV inventory, and UAV energy constraints are subsequently checked. Any quantities modified during repair are rechecked against the affected constraints, and unresolved violations are retained in the constraint violation measure.

For each selected sortie, the decoder calculates aerial travel time and energy using the inherited take-off node, assigned demand point, recovery node, and delivery quantity. Execution times are then propagated from one interval to the next, accounting for ground delivery, launch preparation, travel, aerial delivery, and recovery operations.

The synchronization timeline in Figure 1b illustrates that the completion of an interval depends on both UGV arrival and UAV recovery. Let G_{gk} be the time at which UGV g reaches its next stop, and let V_{agk} be the time at which UAV a reaches the recovery node. The beginning of the next interval is calculated as

$$T_{g,k+1} = \max\left\{G_{gk}, \max_{a \in \mathcal{A}_{gk}^{\text{out}}}\left[\max\{G_{gk}, V_{agk}\} + r_a\right]\right\}, \tag{39}$$

where $\mathcal{A}_{gk}^{\text{out}}$ is the set of UAVs dispatched during interval k, and r_a is the recovery and battery replacement time. If no UAV is dispatched, the recursion reduces to $T_{g,k+1} = G_{gk}$.

Under the assumed safe waiting at recovery nodes and parallel recovery operations, the earlier-arriving vehicle waits until its counterpart arrives, after which recovery and battery replacement can begin. Equation (39) therefore prevents a subsequent sortie from starting before both the UGV and all UAVs assigned to the interval are ready. In the illustrated example, recovery at A must finish before the second sortie starts, and recovery at B must finish before the final interval begins.

Finally, the decoded schedule and resource consumption are used to evaluate the weighted demand completion time, operating cost, maximum normalized workload, and constraint violation, as shown in Figure 1c. For split demand, completion is determined by the last delivery needed to satisfy that demand; thus, h_1 is completed when the second three-unit delivery finishes. Execution times are decoded rather than encoded, allowing the evolutionary search to operate on routing, assignment, and quantity decisions while the decoder handles their temporal coupling.

4.3. Objective Normalization and Decomposition

Because the three objectives have different units, objective values are normalized before decomposition and HV calculation. For objective m, fixed lower and upper bounds L_m and U_m are obtained from a preliminary sampling or from problem-specific analytical bounds. The normalized objective is

$$y_m(x) = \frac{f_m(x) - L_m}{U_m - L_m}, \qquad m \in \{1, 2, 3\}. \tag{40}$$

The bounds remain fixed during one run so that the meaning of an HV gain does not change from generation to generation.

Let $\Lambda = \{\lambda_1, \ldots, \lambda_{N_D}\}$ be a set of positive decomposition directions satisfying

$$\lambda_{im} > 0, \qquad \sum_{m=1}^{3} \lambda_{im} = 1. \tag{41}$$

For direction λ_i, we use the augmented Tchebycheff scalarizing function

$$g_i(x) = \max_{m \in \{1,2,3\}} \frac{y_m(x)}{\lambda_{im}} + \rho \sum_{m=1}^{3} y_m(x), \tag{42}$$

where $\rho > 0$ is a small augmentation coefficient. Each solution in D is associated with one direction. The neighborhood $B(i)$ of direction i consists of the T directions with the smallest Euclidean distance to λ_i.

For a candidate solution x', replacement of the current solution x^i is determined by feasibility first. Specifically,

$$x' \prec_i x^i \tag{43}$$

if one of the following conditions holds:

1. x' is feasible and x^i is infeasible;
2. Both solutions are infeasible and $CV(x') < CV(x^i)$;
3. Both solutions are feasible and $g_i(x') < g_i(x^i)$.

The normalized constraint violation is defined as

$$CV(x) = \sum_{j=1}^{J} \frac{\mathrm{viol}_j(x)}{s_j}, \tag{44}$$

where s_j is a scale associated with constraint j.

4.4. Hypervolume Archive Management

Only feasible non-dominated solutions are stored in the external archive. For a normalized objective vector, let $\boldsymbol{r}$ be a reference point that is worse than all archived solutions in every objective. The hypervolume of a feasible set A is

$$HV(A; \boldsymbol{r}) = \mathrm{vol}\left(\bigcup_{x \in A} \prod_{m=1}^{3} [y_m(x), r_m] \right). \tag{45}$$

In the experiments, the reference point is fixed for each instance. If all normalized values are bounded by one, a practical choice is $\boldsymbol{r} = (1.1, 1.1, 1.1)$.

At the end of each generation, feasible offspring are merged with the current archive and dominated solutions are removed:

$$A \leftarrow ND\big(A \cup Q^{\mathrm{feas}}\big), \tag{46}$$

where $ND(\cdot)$ denotes the non-dominated subset. If the archive exceeds its capacity N_A, the solution with the smallest exclusive HV contribution is deleted. The contribution of solution x is

$$HVC(x \mid A) = HV(A; \boldsymbol{r}) - HV(A \setminus \{x\}; \boldsymbol{r}). \tag{47}$$

Contributions are recomputed after every deletion because the contribution of the remaining solutions changes when the archive changes.

4.5. HV Gain-Guided Direction Adaptation

The archive is also used to provide feedback for adapting the decomposition directions. At the beginning of generation t, the archive is frozen as A_t. For an offspring x' generated for direction i, its feasible HV gain is defined by

$$r_i(x') = \begin{cases} HV(A_t \cup \{x'\}; \boldsymbol{r}) - HV(A_t; \boldsymbol{r}), & x' \text{ is feasible}, \\ 0, & x' \text{ is infeasible}. \end{cases} \tag{48}$$

Using a frozen archive avoids dependence on the order in which offspring are evaluated. The gains of different offspring can overlap and therefore are used as search feedback rather than interpreted as additive generation-wise HV increments.

Within an adaptation window of W generations, the average gain of direction i is

$$\bar{r}_i = \frac{\sum_{x' \in Q_i} r_i(x')}{\max\{1, |Q_i|\}}, \tag{49}$$

where Q_i is the set of offspring generated for direction i. An exponentially smoothed score is maintained as

$$R_i \leftarrow (1-\alpha)R_i + \alpha \bar{r}_i, \qquad 0 < \alpha \leq 1. \tag{50}$$

The denominator in $\bar{r}_i$ includes unsuccessful attempts. Thus, a direction that repeatedly fails to produce feasible improvements receives a lower score.

Direction adaptation is triggered only after every direction has received a minimum number of attempts. Among directions with low smoothed scores, we select a direction that is also redundant in objective space, for example, one whose representative solution is close to another representative or whose local archive density is high. The direction is then moved toward a feasible archive or offspring solution with positive HV gain and insufficient local coverage. Let x^* be the selected target solution. Its target direction is constructed as

$$\lambda_m^* = \frac{y_m(x^*) + \varepsilon}{\sum_{\ell=1}^{3}(y_\ell(x^*) + \varepsilon)}, \qquad m = 1, 2, 3, \tag{51}$$

where ε avoids zero components. The selected direction is updated by

$$\lambda_i \leftarrow (1-\gamma)\lambda_i + \gamma\lambda^*, \qquad 0 < \gamma \leq 1, \tag{52}$$

followed by normalization onto the unit simplex. Boundary directions are protected, and only a small number of directions is modified in one adaptation event. If the candidate target is too close to an existing direction, the update is skipped to avoid excessive direction clustering. After an update, direction neighborhoods are rebuilt and the representative solution of the affected subproblem is selected from already evaluated solutions.

4.6. Problem-Specific Variation and Repair Operators

Generic crossover and mutation can easily break the association between a UGV route and its UAV sorties. HV-ADEA therefore uses variation operators that modify coupled decisions.

Mobile base and sortie adjustment: A UGV stop is inserted, deleted, or replaced, and all UAV sorties attached to the affected interval are decoded again. A sortie may be assigned to another feasible demand point, disabled, or moved to a neighboring interval.

Air–ground quantity transfer: For demand point h, a quantity δ can be transferred between two feasible service actions r and s according to

$$q'_{rh} = q_{rh} - \delta, \qquad q'_{sh} = q_{sh} + \delta, \tag{53}$$

where δ is bounded by the source quantity, residual payload, residual UGV inventory, and residual UAV energy. Demand conservation is restored after every transfer.

Batch splitting and merging: A delivery batch can be divided among multiple feasible UGV or UAV service actions, or two small batches serving the same demand point can be merged. A fixed sortie cost discourages unnecessary fragmentation.

Synchronization improvement: The interval with the largest air–ground waiting time is identified. Its UGV stop, UAV demand point, or delivery quantity is locally modified to reduce the maximum UGV arrival time and UAV recovery time.

A repair procedure is applied in the following sequence after any changes occur: route and associated repairs, then load and energy repairs, followed by inventory and demand repairs, and, finally, the time range check. If a solution remains infeasible after a bounded number of repair attempts, its true CV value is retained and it can only participate in decomposition population search.

4.7. Algorithm

Algorithm 1 summarizes HV-ADEA. The computational budget is measured by the number of objective evaluations so that comparisons with other algorithms remain fair.

Algorithm 1 Hypervolume-Guided Adaptive Decomposition Evolutionary Algorithm (HV-ADEA)

Require: Problem instance, evaluation budget B, decomposition population size N_D, archive capacity N_A, neighborhood size T, adaptation period W
Ensure: Feasible non-dominated archive A

Precompute feasible UGV connections and feasible UAV routes
Generate initial directions $\mathcal{U}$ and neighborhoods $B(i)$
Generate, decode, repair, and evaluate an initial population
Initialize one representative solution for each direction and construct D
$A \leftarrow ND(\text{feasible initial solutions})$
while the number of evaluations is less than B **do**
    Freeze the archive snapshot $A_t \leftarrow A$
    $Q \leftarrow \emptyset$
    for each direction $i = 1, \ldots, N_D$ **do**
        Select parents from $B(i)$, with a small probability of global selection
        Apply coupled crossover and one problem-specific mutation operator
        Decode and repair the offspring x'
        Evaluate $\mathbf{f}(x')$ and $CV(x')$
        Update up to a bounded number of neighboring representatives using $\prec_i$
        Store x' in Q and record $r_i(x')$ using A_t
    end for
    $A \leftarrow ND\left(A \cup Q^{\text{feas}}\right)$
    while $|A| > N_A$ **do**
        Remove the solution with the smallest current HVC from A
    end while
    if an adaptation period has elapsed **then**
        Update R_i using Equation (50)
        Select a few low-reward and redundant directions
        Move selected directions using Equations (51) and (52)
        Rebuild neighborhoods and reselect affected representatives
    end if
end while
return A

4.8. Computational Complexity

Let E be the number of objective evaluations, N_D the decomposition population size, N_A the archive capacity, and $m = 3$ the number of objectives. The decoding cost is dominated by route, sortie, inventory, energy, and time propagation and is approximately linear in the number of encoded service actions. For three objectives, the archive HV and exclusive contribution calculations can be performed efficiently with an exact three-dimensional HV routine. In the worst case, repeated archive deletion requires $O(N_A^2)$ archive operations per generation, in addition to the objective evaluations. Since $m = 3$ is fixed and N_A is bounded, the objective evaluation and decoding costs are expected to dominate for large rescue instances. Although the current HV-ADEA framework employs exact hypervolume

calculations, the repeated evaluation of HV and exclusive HV contributions introduces additional computational overhead. To further improve computational scalability, future work will investigate advanced approximation techniques, such as R2-Based Hypervolume Contribution Approximation [26] and Monte Carlo sampling-based HV estimation [27]. These methods have the potential to reduce computational costs associated with archive maintenance and adaptive direction adjustment. Their effectiveness will be further evaluated in terms of computational efficiency and approximation accuracy.

5. Numerical Experiment

5.1. Test Case Settings

To evaluate HV-ADEA across different problem scales, we generate synthetic instances of centralized UAV–UGV task allocation for post-disaster material distribution. The six configurations in Table 3 specify the numbers of UGVs, UAVs, and demand points, the area size, and the demand range. These quantities are controlled experimental factors. All remaining instance parameters are randomly sampled or calculated from the sampled quantities through the rules described below. Once an instance has been generated, its demands, accessibility conditions, and platform characteristics remain fixed throughout optimization.

Let $n_0 = |\mathcal{N}|$, $m_0 = |\mathcal{G}|$, and L denote the number of demand points, the number of UGVs, and the side length of the disaster area, respectively. We use $\mathcal{U}(a, b)$ for a continuous uniform distribution and $\mathcal{U}_{\text{int}}(a, b)$ for a discrete uniform distribution over the integers from a to b, inclusive. Primitive random draws are independent unless a conditional sampling rule is explicitly stated. Distances, material quantities, time, energy, and costs are expressed in internally consistent normalized units. The numerical ranges define a synthetic benchmark rather than calibrated specifications of particular platforms.

Table 3. MRTA test cases with different problem scales.

Case	UGVs	UAVs	Demand Points	Area Size	Demand per Point
S1	2	4	10	100 × 100	5 ∼ 15
S2	3	6	15	100 × 100	5 ∼ 20
M1	4	8	25	150 × 150	5 ∼ 25
M2	5	10	40	150 × 150	5 ∼ 30
L1	6	12	60	200 × 200	5 ∼ 35
L2	8	16	80	250 × 250	5 ∼ 40

5.1.1. Spatial Distribution, Demands, and Urgency Weights

The disaster area is represented by the square $[0, L] \times [0, L]$. The depot coordinates are independently sampled from $\mathcal{U}(0.4L, 0.6L)$, placing the depot within the central part of the area while allowing its location to vary between instances. The coordinates of each demand point are independently sampled from $\mathcal{U}(0, L)$. The number of additional candidate rendezvous sites is generated as $n_R \sim \mathcal{U}_{\text{int}}(\lceil 0.2n_0 \rceil, \lceil 0.4n_0 \rceil)$, and their coordinates are sampled using the same rule as the demand points. A coordinate draw is rejected if its distance from any previously accepted location is less than $0.01L$.

For configuration c, the demand quantity at point h is generated as $d_h \sim \mathcal{U}(5, d_c^{\max})$, where $d_c^{\max}$ equals 15, 20, 25, 30, 35, and 40 for S1, S2, M1, M2, L1, and L2, respectively. Demand quantities are continuous, consistent with the divisible commodity formulation. The urgency weight is sampled as $w_h \sim \mathcal{U}_{\text{int}}(1, 5)$. Demand quantities and urgency weights are sampled independently, allowing both small and large demands to receive different urgency levels.

5.1.2. Ground Accessibility and Road Network Generation

An instance-specific ground accessibility probability is sampled as $p_G \sim \mathcal{U}(0.6, 0.8)$. Each demand point is classified as ground-accessible with probability p_G; otherwise, it can only receive aerial deliveries. The accessibility labels are resampled until both categories contain at least one demand point. The stopping node set $\mathcal{V}$ comprises the depot, ground-accessible demand points, and candidate rendezvous sites.

An undirected candidate road network is constructed by Delaunay triangulation of the locations in $\mathcal{V}$. The road damage probability is sampled as $p_D \sim \mathcal{U}(0.15, 0.35)$, and each candidate road edge is independently removed with probability p_D. Edge removal draws are repeated until at least one edge has been removed and the retained network remains connected. Consequently, ground-accessible locations can be reached from the depot, while road damage introduces detours and additional travel requirements.

Each retained road edge e receives a terrain multiplier $\xi_e \sim \mathcal{U}(1.0, 1.4)$. Its effective length is ξ_e times its Euclidean length. Let D^G_{ij} denote the shortest path distance between nodes i and j under these effective edge lengths. An admissible ground connection represents this precomputed path rather than an individual road edge. The same physical road network is used by all UGVs, while platform-specific speeds and cost rates produce different travel parameters.

5.1.3. Fleet Composition and Platform Parameters

UAVs are randomly assigned to supporting UGVs before optimization. Specifically, the UAV indices are randomly permuted, one UAV is assigned to each UGV, and every remaining UAV is independently assigned to a uniformly selected UGV. This procedure ensures that each UGV supports at least one UAV while allowing the numbers of UAVs carried by different UGVs to vary. The resulting sets $\mathcal{A}_g$ remain fixed during the mission.

Platform parameters are generated according to the distributions below. Each platform-specific quantity is sampled separately for the corresponding robot, whereas the common aerial energy price c^A is sampled once per instance.

5.1.4. Travel, Energy, and Cost Coefficients

Ground travel times and operating costs are calculated as

$$t^G_{gij} = \frac{D^G_{ij}}{v^G_g}, \qquad c^G_{gij} = \gamma_g D^G_{ij}.$$

Self-loops have zero travel time and zero travel cost. All pairs of sampled locations have admissible aerial connections, and UAV travel follows Euclidean links. For sortie $s = (i, h, j)$, let D^A_{ih} and D^A_{hj} denote the corresponding Euclidean distances. Aerial travel times are calculated as

$$t^{\text{out}}_{as} = \frac{D^A_{ih}}{v^A_a}, \qquad t^{\text{in}}_{as} = \frac{D^A_{hj}}{v^A_a}.$$

The coefficients of the linear sortie energy model are generated from the sampled platform parameters:

$$e^0_{as} = \varepsilon_a + \alpha_a\left(t^{\text{out}}_{as} + t^{\text{in}}_{as} + s^0_a\right),$$

$$\kappa_{as} = \beta_a t^{\text{out}}_{as} + \alpha_a \rho_a.$$

Here, α_a represents baseline energy consumption per time unit, and β_a represents additional flight energy consumption per time unit and material unit. The payload-related flight term applies to the outbound leg because the shipment is unloaded before recovery. This construction preserves the relationship between flight time, shipment quantity, and energy consumption.

A candidate sortie is retained only if its ground connection is admissible and $e^0_{as} < B_a$, allowing a positive shipment quantity. Its maximum feasible delivery quantity is

$$\bar{q}_{as} = \min\left\{Q_a, d_h, \frac{B_a - e^0_{as}}{\kappa_{as}}\right\}.$$

5.1.5. Conditional Generation of Inventory and Aggregate Energy Budgets

To ensure that every accepted instance admits a feasible solution, a randomized reference plan is constructed before generating the mission-level resource budgets. For each aerial-only demand point, at least one UAV–site pair (a, i), with $i \in \mathcal{U}$, must satisfy $e^0_{a,(i,h,i)} + \kappa_{a,(i,h,i)} Q_a \le B_a$. An instance candidate that fails this condition is rejected and regenerated.

For each ground-accessible demand point, the reference service mode is selected as ground or aerial delivery with equal probability. A ground delivery is assigned to a uniformly selected UGV. An aerial delivery is assigned by uniformly selecting an eligible UAV–site pair satisfying the above energy condition. Aerial-only demand points always use aerial delivery. A demand assigned to UAV a is divided into $\lceil d_h/Q_a \rceil$ equal shipments and served by successive stationary sorties from the selected site.

The service actions assigned to each UGV are randomly ordered. Each reference route starts at the depot, visits its assigned service locations using the precomputed ground paths, and returns to the depot. Aerial shipments are executed sequentially at their selected sites, with launch preparation, service, recovery, and battery exchange included. The synchronized decoder determines the execution times.

Let $\hat{I}_g$ be the total material quantity delivered by UGV g and its UAVs, and let $\hat{E}_g$ be their total UAV sortie energy consumption in the reference plan. The usable UGV material capacity and aggregate UAV energy budget are generated as

$$Q_g = \lambda^Q_g \max\left\{\hat{I}_g, \frac{\sum_h d_h}{2m}\right\}, \qquad \lambda^Q_g \sim \mathcal{U}(1.05, 1.25),$$

$$B_g = \lambda^B_g \max\left\{\hat{E}_g, \sum_{a \in A_g} B_a\right\}, \qquad \lambda^B_g \sim \mathcal{U}(1.05, 1.30).$$

These conditional distributions provide randomized resource margins while ensuring sufficient initial inventory and carried UAV energy for the reference plan. The reference plan establishes feasibility but does not constrain the optimized assignments, routes, or shipment quantities. It is not supplied to any algorithm as an initial solution.

5.1.6. Planning Limits, Workload References, and Reproducibility

Let $\widehat{T}$ denote the latest depot return time in the reference plan, and let $\widehat{K}$ denote the largest number of operating intervals used by any reference UGV route. The planning horizon and interval limit are generated as

$$H = \lambda^H \widehat{T}, \qquad \lambda^H \sim \mathcal{U}(1.10, 1.30),$$

$$K = \widehat{K} + \Delta K, \qquad \Delta K \sim \mathcal{U}_{\text{int}}(2, 5).$$

Unused intervals can be padded by repeated depot stops. Platform-specific workload references are generated as

$$\overline{W}_g = \omega_g H, \qquad \omega_g \sim \mathcal{U}(0.6, 0.9),$$

$$\overline{W}_a = \omega_a H, \qquad \omega_a \sim \mathcal{U}(0.3, 0.6).$$

These reference budgets normalize active workloads and do not impose additional hard limits. The time relaxation constant M is calculated from the generated instance using Equation (27), ensuring that it remains valid for all candidate sorties.

Instance generation uses the PCG64 pseudorandom number generator, with seed $100{,}000 + 1000c + j$, where $c \in \{1, \ldots, 6\}$ follows the configuration order in Table 3, and $j \in \{1, \ldots, 10\}$ identifies the instance. Rejected draws consume the same random stream without resetting the generator. The accepted parameter values, accessibility labels, road network, and travel matrices are retained together with the seed. Each algorithm is executed independently 30 times per instance using a common predefined list of search seeds. Instance generation randomness and algorithm search randomness are handled separately, allowing the experiments to account for both variation between problem instances and stochastic variation between algorithm runs. Each algorithm is executed independently for 30 runs on every instance using different random seeds. The six test configurations used in the experiments are summarized in Table 4.

Table 4. Platform parameter generation rules.

Parameter	Generation Rule
UGV travel speed v_g^G	$\mathcal{U}(1.0, 2.0)$
UAV travel speed v_a^A	$\mathcal{U}(4.0, 8.0)$
UAV payload capacity Q_a	$\mathcal{U}(2.0, 5.0)$
Usable UAV sortie energy budget B_a	$\mathcal{U}(15.0, 30.0)$
Fixed ground service time s_g^0	$\mathcal{U}(0.5, 1.5)$
Ground service time per material unit ρ_g	$\mathcal{U}(0.02, 0.06)$
Fixed aerial service time s_a^0	$\mathcal{U}(0.2, 0.6)$
Aerial service time per material unit ρ_a	$\mathcal{U}(0.03, 0.08)$
UAV launch preparation time ℓ_a	$\mathcal{U}(0.1, 0.4)$
UAV recovery and battery exchange time r_a	$\mathcal{U}(0.2, 0.5)$
UAV baseline energy rate α_a	$\mathcal{U}(0.8, 1.2)$
UAV payload-related energy rate β_a	$\mathcal{U}(0.02, 0.06)$
Fixed take-off and landing energy ε_a	$\mathcal{U}(0.2, 0.5)$
UGV cost per effective distance unit γ_g	$\mathcal{U}(0.8, 1.5)$
Cost per UAV energy unit c^A	$\mathcal{U}(0.5, 1.0)$
Fixed cost per UAV sortie c_a^S	$\mathcal{U}(1.0, 3.0)$

5.2. Comparative Algorithm Settings

HV-ADEA is compared with five representative multi-objective evolutionary algorithms: NSGA-II, CCMO, BiCo, EMCMO, and C3M. NSGA-II is included as a classical baseline, while the other four methods were published between 2021 and 2023 and explicitly address constrained multi-objective optimization. These methods provide complementary baselines for evaluating the search performance of HV-ADEA under payload, inventory, energy, and aerial–ground synchronization constraints.

1. NSGA-II [28]: This algorithm combines non-dominated sorting with crowding distance estimation. Its constrained version is adopted, giving priority to feasible solutions and using constraint violation to compare infeasible solutions. It serves as a conventional dominance-based baseline.
2. CCMO [29]: This coevolutionary framework maintains a population for the original constrained problem and an auxiliary population that ignores constraints. Offspring sharing allows the two populations to exchange search information. It is included to examine the effectiveness of auxiliary exploration in constrained search spaces.
3. BiCo [30]: This method uses bidirectional coevolution to coordinate complementary search processes for constrained multi-objective optimization. It provides a baseline for

assessing whether information exchange between different search directions improves feasible front approximation.

4. EMCMO [31]: This framework treats constrained optimization and an auxiliary optimization task within an evolutionary multitasking scheme. Knowledge transfer between tasks supports the search for promising solutions. It is selected to evaluate the benefits of task-assisted search on the proposed MRTA problem.
5. C3M [32]: This algorithm uses multiple evolutionary stages to handle problems with multiple constraints. It is included to evaluate the performance of staged constraint handling when routing, payload, energy, and synchronization requirements interact.

All methods are adapted to the same hybrid representation $x = (R, S, Q)$ and use the same synchronized decoder, objective functions, and constraint definitions. The decoder returns both the objective vector and the individual constraint violations. Constraint scaling and equality tolerances are identical across methods, while each algorithm retains its original mating selection, environmental selection, constraint-handling rules, and population or archive interactions.

The baseline algorithms use a common set of representation-compatible variation operators: route segment crossover, stop insertion or relocation, UAV assignment mutation, and delivery quantity perturbation. Repeated UGV stops remain admissible. A common bounded repair procedure is applied to all methods, with identical repair limits. Unresolved violations are retained for the algorithms' native constraint-handling mechanisms. HV-ADEA additionally employs its proposed adaptive search mechanism and domain-specific variation operators.

The nominal population size is set to $N_{\text{pop}} = 100$. For methods maintaining multiple populations or archives, their original structures are preserved and their actual sizes are reported. Computational budgets are controlled by the total number of function evaluations rather than by the number of generations. The evaluation limits are set to 50,000, 100,000, and 200,000 for small-, medium-, and large-scale instances, respectively. Evaluations from all populations, auxiliary tasks, initialization, and any objective-based repair or local search are included in the same budget. Reusing an already evaluated solution does not incur an additional evaluation.

Each algorithm is executed independently 30 times on each instance using the same predefined list of random seeds. The same initialization procedure is used across algorithms. Algorithm-specific parameters follow the original publications unless explicitly stated otherwise. Any parameter tuning is conducted on separate training instances with an equal tuning budget. At termination, only solutions feasible for the original MRTA problem are retained for non-dominated set evaluation. Runs without feasible solutions are recorded as failures. Wall-clock runtime is also reported on the same computing platform.

5.3. Performance Metrics

The performance of HV-ADEA and the comparative algorithms is evaluated using the hypervolume (HV) and inverted generational distance (IGD) indicators. These two metrics measure complementary aspects of multi-objective optimization: HV evaluates the convergence and distribution of the obtained non-dominated solutions, whereas IGD measures the distance between the obtained approximation set and a reference Pareto front.

Before calculating the indicators, all objective values are normalized using the ideal and nadir points of the reference set. For the j-th objective, the normalized value of solution x is defined as

$$\bar{f}_j(x) = \frac{f_j(x) - z_j^{\text{ideal}}}{z_j^{\text{nadir}} - z_j^{\text{ideal}}}, \tag{54}$$

where z_j^{ideal} and z_j^{nadir} denote the ideal and nadir values, respectively. The same normalization bounds are used for all algorithms and independent runs.

5.3.1. Hypervolume

Let A denote the feasible non-dominated approximation set obtained by an algorithm, and let r be a reference point that is dominated by all normalized solutions in A. The hypervolume is defined as

$$HV(A) = \text{vol}\left(\bigcup_{a \in A} [\bar{\boldsymbol{f}}(a), \boldsymbol{r}] \right), \tag{55}$$

where $\text{vol}(\cdot)$ denotes the Lebesgue measure of the objective space and

$$[\bar{\boldsymbol{f}}(a), \boldsymbol{r}] = \prod_{j=1}^{M} [\bar{f}_j(a), r_j].$$

In this study, the reference point is selected as

$$\boldsymbol{r} = (1.1, 1.1, \ldots, 1.1), \tag{56}$$

after objective normalization. A larger HV value indicates that the approximation set is closer to the ideal point, covers a larger portion of the objective space, and has better diversity. Solutions that violate any original MRTA constraint are excluded before HV calculation.

5.3.2. Inverted Generational Distance

Let P^* denote the reference Pareto front and let A denote the feasible non-dominated approximation set produced by an algorithm. The IGD metric is defined as

$$IGD(A, P^*) = \frac{1}{|P^*|} \sum_{\boldsymbol{p} \in P^*} \min_{\boldsymbol{a} \in A} \|\boldsymbol{p} - \boldsymbol{a}\|_2, \tag{57}$$

where $\|\cdot\|_2$ denotes the Euclidean distance in the normalized objective space.

A smaller IGD value indicates that the obtained solution set is closer to the reference Pareto front and provides better coverage. Thus, HV is expected to be maximized, whereas IGD is expected to be minimized.

5.3.3. Construction of the Reference Pareto Front

Since the exact Pareto front is unavailable for the considered large-scale MRTA instances, a practical reference front is constructed separately for each test case. First, the feasible non-dominated solutions from all algorithms and all independent runs are pooled. Duplicate solutions are removed, and the remaining solutions are filtered again by Pareto dominance. The resulting set is denoted by

$$P^{\text{ref}} = ND\left(\bigcup_{m=1}^{N_{\text{alg}}} \bigcup_{r=1}^{N_{\text{run}}} A_{m,r} \right), \tag{58}$$

where $A_{m,r}$ is the final feasible non-dominated set obtained by algorithm m in run r, and $ND(\cdot)$ denotes the non-dominated filtering operation. The reference front used in Equation (57) is obtained by uniformly sampling at most N_{ref} points from P^{ref} when the set is too large.

The ideal and nadir points used in Equation (54) are calculated from P^{ref}. To avoid bias, the reference front is constructed independently for each problem instance and is kept fixed when evaluating all algorithms on that instance.

5.4. Experimental Results and Analysis

This subsection compares HV-ADEA with NSGA-II, CCMO, BiCo, EMCMO, and C3M on the six test cases defined in Section 5.1. The comparison focuses on four aspects: numerical performance in terms of HV and IGD, statistical significance, computational efficiency, and the distribution of the obtained non-dominated solutions.

For each algorithm and test case, 30 independent runs are performed. The mean and standard deviation of HV and IGD are reported. A larger HV value and a smaller IGD value indicate better performance.

As shown in Tables 5 and 6, HV-ADEA achieves competitive performance across all six test cases. On the small-scale instances S1 and S2, most algorithms are able to obtain relatively high-quality approximation sets. The performance difference is therefore mainly reflected in the diversity of the solutions and the stability over independent runs.

As the problem size increases from S1 to L2, the performance gap between the algorithms becomes more evident. The number of routing, assignment, and split delivery decisions increases simultaneously, which enlarges the feasible search space. The constraint interactions between UGV payload, UAV energy, inventory, and recovery synchronization also make it more difficult to generate feasible offspring. HV-ADEA maintains a relatively high HV and a relatively low IGD on the medium- and large-scale cases, indicating that its search mechanism is effective for both convergence and diversity.

The improvement in HV suggests that HV-ADEA obtains solutions that cover a larger portion of the objective space. The corresponding IGD results further indicate that these solutions are close to the reference Pareto front rather than being concentrated in only one trade-off region. This property is important for the proposed emergency distribution problem because decision makers may prefer different compromises between service completion time, operating cost, and workload balance.

The running time is measured on the same computing platform. For each test case, the reported value is the average wall-clock time over 30 independent runs. The function evaluation budget is identical for all algorithms, including evaluations used by auxiliary populations, archives, and repair procedures. This setting provides a fair comparison of computational efficiency.

As shown in Figure 2, the running time generally increases with the number of demand points and robots. Algorithms with auxiliary populations or multiple evolutionary stages may require additional objective evaluations and environmental selection operations. HV-ADEA may have a higher per-generation computational cost because of its adaptive indicators and domain-specific operators. Such an overhead is acceptable if it produces a clear improvement in HV and IGD. The practical efficiency is therefore evaluated jointly using solution quality and running time.

To investigate the search behavior of the compared algorithms, we examine the evolution of both HV and IGD with the number of function evaluations (FEs) on the six test cases. The trajectories complement the final performance comparisons by revealing early-stage progress, intermediate plateaus, and late-stage improvements. Higher HV values indicate better approximation set quality in terms of convergence and objective space coverage, whereas lower IGD values indicate a smaller average distance from the reference front points to the obtained solution set. Using both indicators allows a more comprehensive assessment because their rankings need not coincide. Within each test case, consistent objective normalization, a fixed HV reference point, and a fixed IGD reference set are required throughout the comparison. The results are shown in Figures 3 and 4, respectively.

Table 5. HV results of different algorithms on six test cases.

Case	NSGA-II	CCMO	BiCo	EMCMO	C3M	HV-ADEA
S1	9.1901×10^{-1} (5.15×10^{-3}) $\approx$	9.2975×10^{-1} (4.56×10^{-3}) +	6.2436×10^{-1} (6.38×10^{-2}) −	**9.3688** $\times 10^{-1}$ (**5.23** $\times 10^{-3}$) +	3.5986×10^{-1} (2.53×10^{-2}) −	9.2443×10^{-1} (5.31×10^{-3})
S2	**9.3039** $\times 10^{-1}$ (**1.73** $\times 10^{-3}$) +	9.1852×10^{-1} (2.11×10^{-3}) $\approx$	9.2111×10^{-1} (4.39×10^{-3}) $\approx$	9.2825×10^{-1} (1.67×10^{-3}) +	9.2791×10^{-1} (1.47×10^{-3}) +	9.1969×10^{-1} (4.40×10^{-3})
M1	4.0139×10^{-1} (1.78×10^{-3}) $\approx$	3.9801×10^{-1} (1.75×10^{-3}) −	3.5843×10^{-1} (9.70×10^{-3}) −	3.5891×10^{-1} (7.17×10^{-3}) −	3.5539×10^{-1} (6.84×10^{-3}) −	**4.0159** $\times 10^{-1}$ (**2.66** $\times 10^{-3}$)
M2	5.4227×10^{-1} (2.82×10^{-3}) −	5.1926×10^{-1} (4.36×10^{-3}) −	5.2332×10^{-1} (5.90×10^{-3}) −	5.3372×10^{-1} (2.51×10^{-3}) −	4.9103×10^{-1} (4.09×10^{-3}) −	**5.5213** $\times 10^{-1}$ (**2.80** $\times 10^{-3}$)
L1	5.0073×10^{-1} (3.15×10^{-3}) −	4.9251×10^{-1} (4.72×10^{-3}) −	4.8933×10^{-1} (2.54×10^{-3}) −	**5.0800** $\times 10^{-1}$ (**3.01** $\times 10^{-3}$) $\approx$	4.7617×10^{-1} (6.69×10^{-3}) −	5.0708×10^{-1} (3.93×10^{-3})
L2	4.8775×10^{-1} (1.24×10^{-2}) $\approx$	4.6991×10^{-1} (1.27×10^{-2}) −	5.0878×10^{-1} (1.32×10^{-2}) $\approx$	4.8836×10^{-1} (1.14×10^{-2}) $\approx$	**5.1752** $\times 10^{-1}$ (**8.00** $\times 10^{-3}$) +	4.9920×10^{-1} (1.83×10^{-2})
+/ − / ≈	1/2/3	1/4/1	0/4/2	2/2/2	2/4/0	

Table 6. IGD results of different algorithms on six test cases.

Case	NSGA-II	CCMO	BiCo	EMCMO	C3M	HV-ADEA
S1	2.8131×10^{-1} (2.89×10^{-2}) −	2.1614×10^{-1} (6.81×10^{-3}) $\approx$	1.1169 (6.40×10^{-2}) −	**1.8833** $\times 10^{-1}$ (**2.76** $\times 10^{-2}$) $\approx$	1.3608 (6.63×10^{-2}) −	2.0650×10^{-1} (1.32×10^{-2})
S2	2.8314×10^{-1} (3.15×10^{-2}) −	2.1583×10^{-1} (1.11×10^{-2}) −	1.8039×10^{-1} (7.04×10^{-3}) +	1.8042×10^{-1} (8.18×10^{-3}) +	**1.7887** $\times 10^{-1}$ (**5.20** $\times 10^{-3}$) +	1.9265×10^{-1} (9.39×10^{-3})
M1	8.1169×10^{-2} (8.93×10^{-3}) −	1.0399×10^{-1} (1.39×10^{-2}) −	1.2940×10^{-1} (1.94×10^{-2}) −	1.5178×10^{-1} (1.47×10^{-2}) −	1.5279×10^{-1} (1.43×10^{-2}) −	**7.1514** $\times 10^{-2}$ (**5.03** $\times 10^{-3}$)
M2	2.8583×10^{-1} (9.00×10^{-3}) −	2.7195×10^{-1} (9.30×10^{-3}) −	2.3887×10^{-1} (9.97×10^{-3}) −	2.3850×10^{-1} (6.89×10^{-3}) −	2.6380×10^{-1} (6.10×10^{-3}) −	**2.3030** $\times 10^{-1}$ (**3.44** $\times 10^{-3}$)
L1	3.1160×10^{-1} (1.69×10^{-2}) −	2.7728×10^{-1} (7.18×10^{-3}) −	2.5719×10^{-1} (9.69×10^{-3}) −	2.4001×10^{-1} (4.40×10^{-3}) $\approx$	2.5166×10^{-1} (6.60×10^{-3}) −	**2.3662** $\times 10^{-1}$ (**3.36** $\times 10^{-3}$)
L2	3.0732×10^{-1} (1.54×10^{-2}) −	3.0716×10^{-1} (1.95×10^{-2}) −	2.5617×10^{-1} (1.16×10^{-2}) $\approx$	2.6411×10^{-1} (9.86×10^{-3}) $\approx$	**2.3955** $\times 10^{-1}$ (**6.51** $\times 10^{-3}$) +	2.5891×10^{-1} (1.28×10^{-2})
+/ − / ≈	0/6/0	0/5/1	1/4/1	1/2/3	2/4/0	

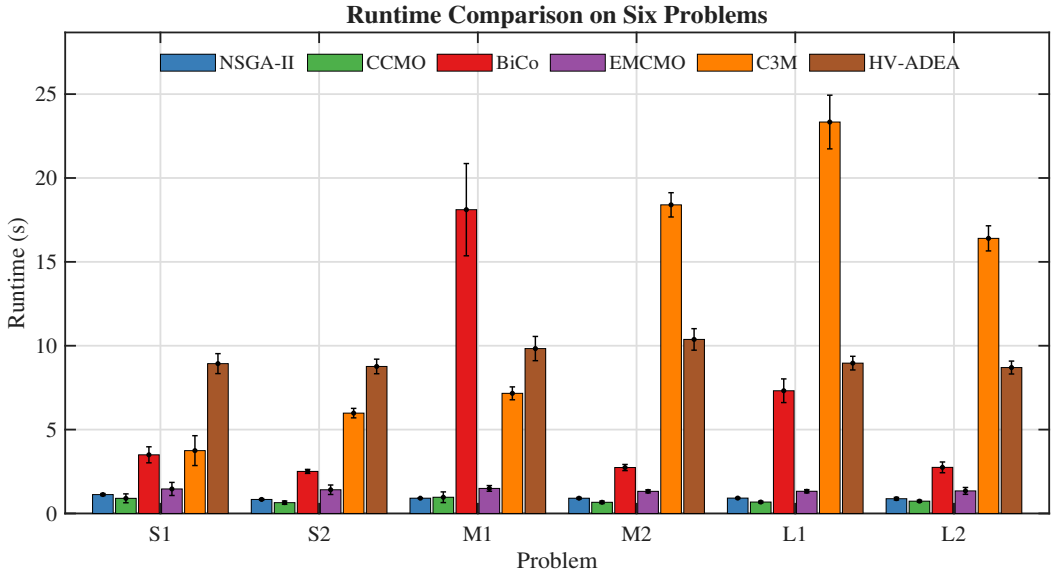
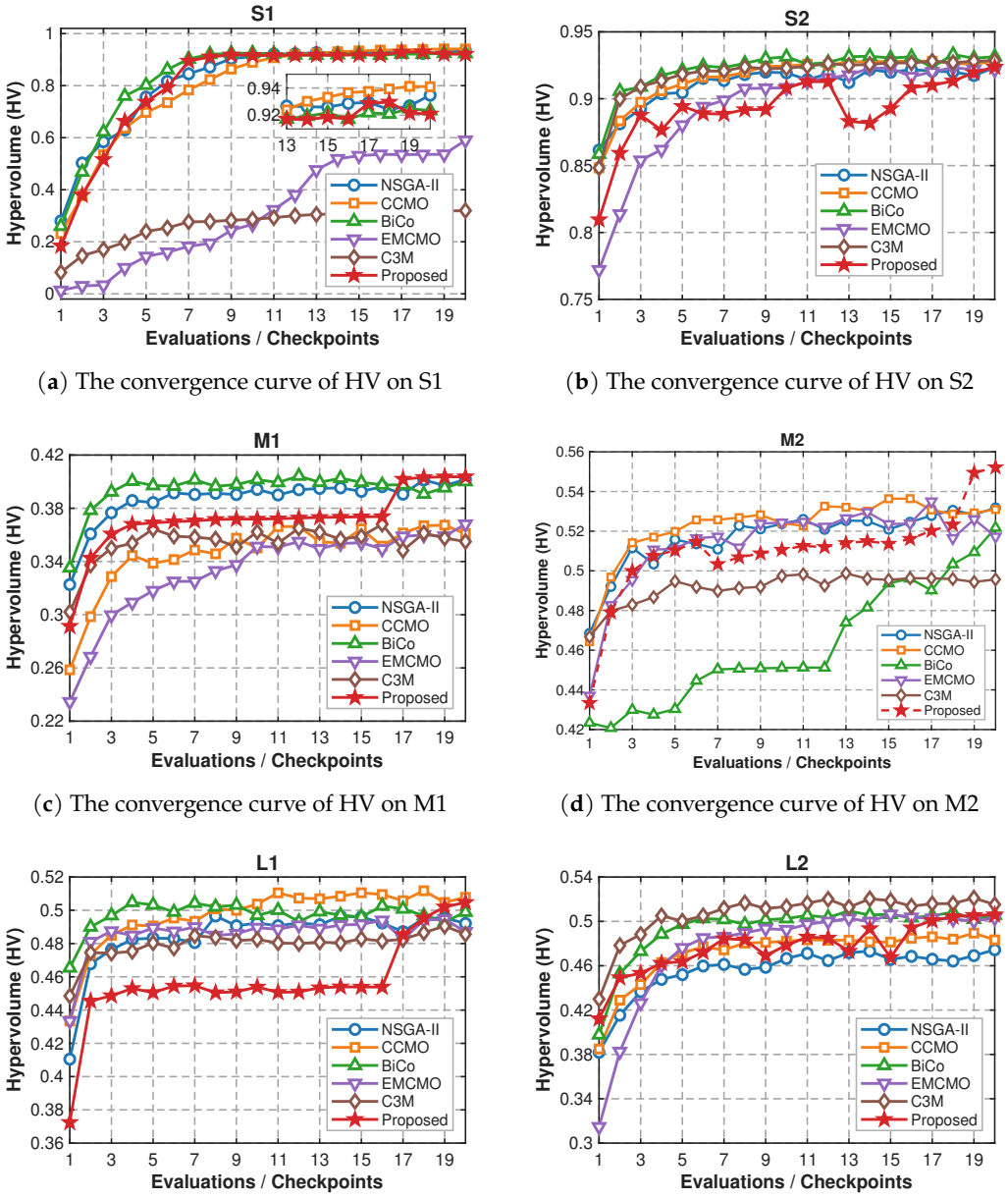


Figure 2. Average running time in seconds on the six test cases.

On S1, BiCo exhibits rapid early improvement in HV, while CCMO improves more gradually and ultimately achieves the highest HV and lowest IGD, with final values of 0.9409 and 0.1587, respectively. HV-ADEA reaches a final HV of 0.9209, below those of CCMO, NSGA-II, and BiCo. However, its final IGD of 0.2034 is the second lowest among all algorithms, outperforming NSGA-II and BiCo despite their higher HV values. This difference illustrates the complementary information provided by the two indicators. On S2, HV-ADEA exhibits intermediate fluctuations followed by recovery, reaching a final HV of 0.9237 and an IGD of 0.1914. BiCo achieves the highest final HV of 0.9314, but its final IGD of 0.3208 is the largest among the compared methods. C3M and CCMO instead obtain the lowest final IGD values. Thus, neither the HV trajectories nor the IGD trajectories support a consistent advantage of HV-ADEA on the small-scale cases.

On M1, BiCo makes rapid early progress in both indicators, whereas HV-ADEA experiences an extended plateau, with HV remaining near 0.37 and IGD near 0.14. A marked improvement occurs late in the search: its HV increases from 0.3737 to 0.4019 between the sixteenth and seventeenth checkpoints, accompanied by an IGD decrease from 0.1352 to 0.0699. HV-ADEA eventually achieves the highest final HV of 0.4037 and the lowest final IGD of 0.0684. The simultaneous improvement in both indicators provides evidence of improved approximation set quality following the plateau. On M2, HV-ADEA also exhibits late-stage improvement and attains a higher final HV than BiCo. Its HV reaches 0.5522, while its IGD decreases to 0.2349. These trajectories indicate that additional evaluations continue to improve the obtained solution set near the end of the search.

On L1, HV-ADEA initially trails behind the competing algorithms in both indicators and makes limited progress during the intermediate stage. Its performance improves substantially over the final four checkpoints: HV increases from 0.4539 at the sixteenth checkpoint to 0.5047 at termination, while IGD decreases from 0.3063 to 0.2320. HV-ADEA finishes second in HV, slightly below CCMO at 0.5078, but achieves the lowest final IGD. Consequently, its final solution set offers competitive dominated volume coverage together with the smallest average distance from the reference front points among the compared methods.



(**a**) The convergence curve of HV on S1

(**b**) The convergence curve of HV on S2

(**c**) The convergence curve of HV on M1

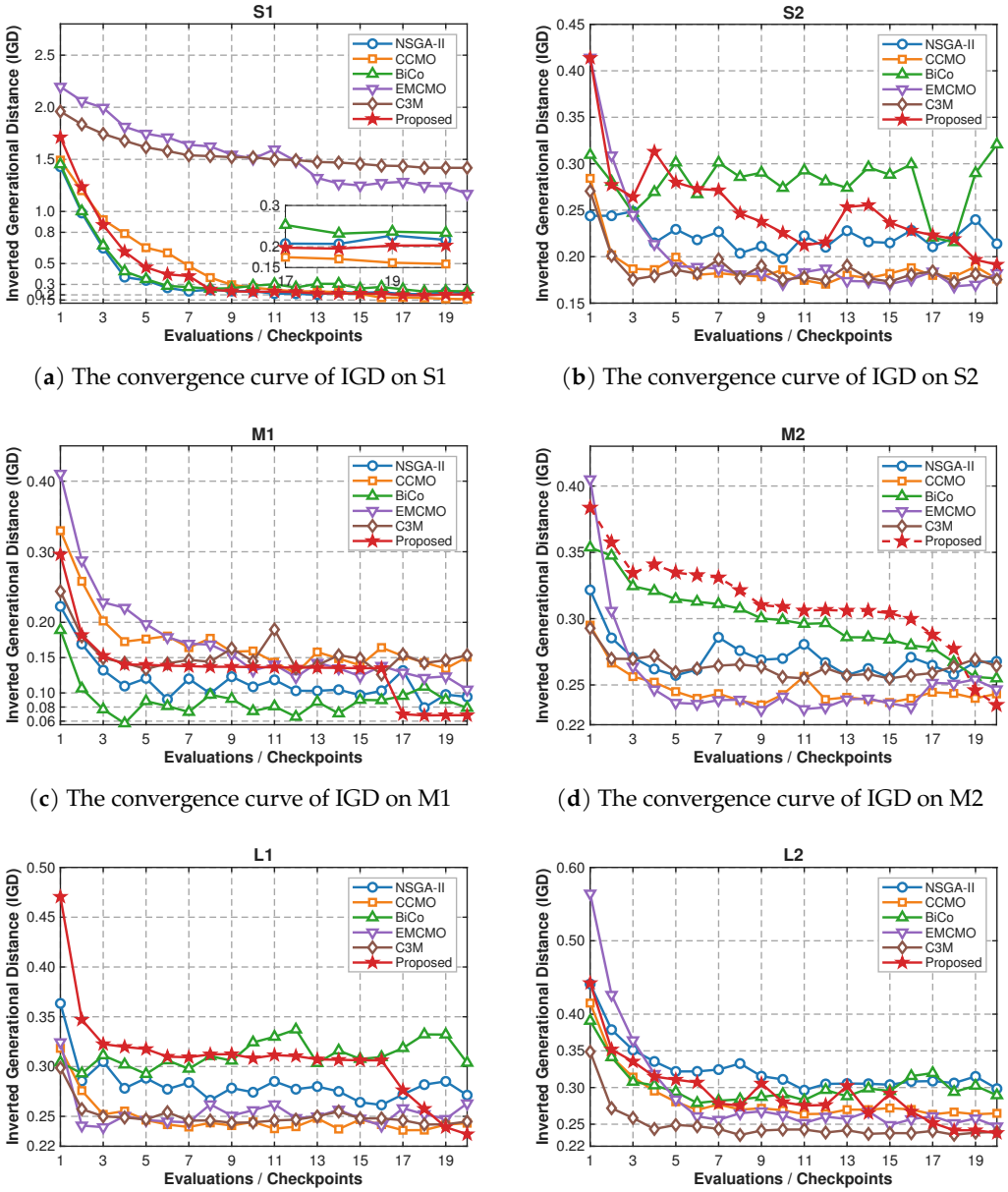
(**d**) The convergence curve of HV on M2

(**e**) The convergence curve of HV on L1

(**f**) The convergence curve of HV on L2

Figure 3. Evolution of HV with the number of function evaluations for the six algorithms on (**a**) S1, (**b**) S2, (**c**) M1, (**d**) M2, (**e**) L1, and (**f**) L2. Higher values indicate better performance.

On L2, C3M maintains the highest HV throughout the recorded search and finishes at 0.5152. HV-ADEA exhibits intermediate fluctuations but continues to improve late in the search, reaching a final HV of 0.5060 and ranking second. In terms of IGD, C3M reaches a relatively low level early, whereas HV-ADEA improves more gradually and ultimately obtains the lowest final value of 0.2381, just below C3M at 0.2394. This small numerical difference should be distinguished from statistical superiority. The trajectories suggest that HV-ADEA remains capable of improving solution quality at later evaluation stages, although it does not match C3M's early search performance on this case.



(**a**) The convergence curve of IGD on S1

(**b**) The convergence curve of IGD on S2

(**c**) The convergence curve of IGD on M1

(**d**) The convergence curve of IGD on M2

(**e**) The convergence curve of IGD on L1

(**f**) The convergence curve of IGD on L2

Figure 4. Evolution of IGD with the number of function evaluations for the six algorithms on (**a**) S1, (**b**) S2, (**c**) M1, (**d**) M2, (**e**) L1, and (**f**) L2. Lower values indicate better performance.

Overall, HV-ADEA's strongest observed feature is its late-stage improvement on several medium- and large-scale cases, rather than uniformly rapid initial progress. It achieves the best final values for both indicators on M1 and combines the second-highest final HV with the lowest final IGD on L1 and L2. Its less competitive small-scale results and intermediate plateaus also reveal opportunities to improve early search efficiency. The joint HV and IGD analysis therefore supports a case-dependent assessment of the algorithm, while statistical comparisons and ablation experiments are needed to establish the reliability of the differences and the contributions of individual mechanisms.

Finally, this paper visually compares the distribution of the solution sets obtained by each algorithm. Figure 5 presents the distribution of solution sets for NSGA-II, BiCo, EMCMO, C3M, CCMO, and HV-ADEA. The gray dots represent the reference Pareto front (PF), and the blue dots represent the solutions obtained by each algorithm in a typical run. Ideally, the solutions obtained by the algorithms should be as close as possible to the PF,

while covering different regions of the PF and maintaining a good distribution uniformity. Therefore, the search performance of different algorithms can be qualitatively compared in terms of the degree of fit with the reference PF, coverage range, and distribution uniformity.

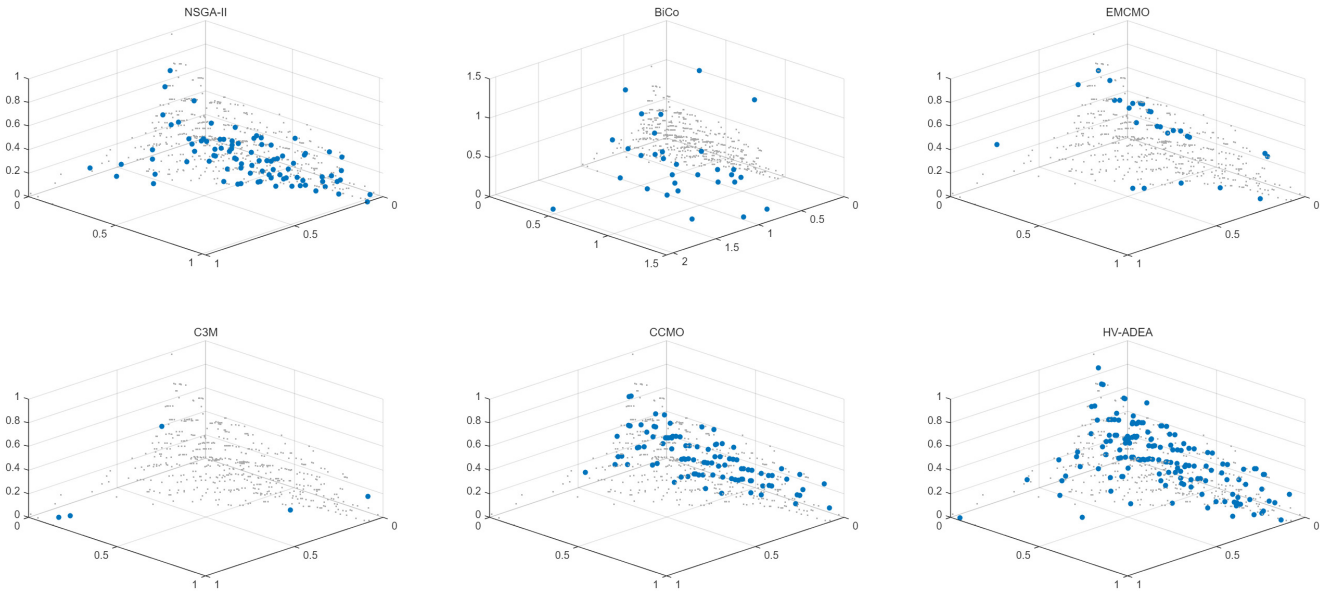


Figure 5. The solution distribution of all algorithms on the M1 test cases.

It can be observed that the algorithms exhibit clear differences in their solution distributions over the PF. NSGA-II is able to identify a certain number of valid solutions and cover several regions of the reference PF. However, its solutions tend to cluster in some local regions, while several solutions remain noticeably distant from the reference PF, indicating limitations in both coverage and distribution uniformity within the complex solution space. The solutions obtained by BiCo are relatively sparse, with some solutions located far from the reference PF and insufficient coverage of different PF regions. EMCMO is able to approximate the reference PF well in certain regions; nevertheless, its overall solution distribution is relatively discontinuous, with several regions left uncovered and a small number of solutions deviating from the PF.

In contrast, C3M obtains only a limited number of effective solutions for this problem, with the resulting solutions distributed over only a few regions of the reference PF. Its relatively low coverage suggests that its search capability is significantly restricted on this problem. CCMO achieves comparatively better performance, as most of its solutions are located close to the reference PF and its coverage is broader than that of NSGA-II, BiCo, EMCMO, and C3M. Nevertheless, some local clustering can still be observed, and several regions of the reference PF remain insufficiently covered.

5.5. Discussion

5.5.1. Interaction of Archive Selection, Direction Adaptation, and Problem-Specific Variation

The approximation behavior observed for HV-ADEA can be interpreted through the complementary roles of archive selection, direction adaptation, and problem-specific variation. These mechanisms respectively influence which solutions are retained, where subsequent search is directed, and how alternative delivery plans are generated.

First, hypervolume contribution-based archive truncation directly considers the additional objective space volume represented by each solution. According to Equation (47), deleting the solution with the smallest exclusive contribution causes the smallest immediate

hypervolume loss among the possible single-solution deletions from the current archive. Solutions with strongly overlapping dominated regions may provide limited additional coverage, whereas solutions extending the covered region can receive larger contributions. This selection pressure can reduce redundant archive members while retaining different compromises among demand completion time, operating cost, and normalized workload. However, favorable hypervolume coverage does not necessarily imply uniformly spaced solutions along the front.

Second, hypervolume information also influences future search through decomposition direction adaptation. As described in Section 4.5, directions with low smoothed feasible gains are considered for adjustment when they are also redundant in objective space. Their targets are feasible solutions providing positive hypervolume gains and insufficient local coverage. Archive filtering selects among solutions already generated, whereas direction adaptation changes the subproblems guiding subsequent offspring generation. The coverage checks, protection of boundary directions, and restriction on the number of modified directions are intended to limit excessive concentration of search effort.

Third, the variation operators in Section 4.6 address the dependencies specific to UAV–UGV cooperation. Joint mobile base and sortie adjustments coordinate changes to ground stops and aerial assignments. Quantity transfer and splitting/merging operators explore alternative allocations with different service time and energy requirements. Synchronization-oriented modifications target waiting bottlenecks whose delays can propagate to subsequent deliveries. These operators provide structured ways to explore alternative trade-offs within the coupled routing, allocation, and scheduling problem.

The representation, synchronized decoder, and common bounded repair procedure are shared across the compared algorithms. They provide a consistent basis for evaluation. The interpretation of relative performance therefore focuses on the additional archive selection, direction adaptation, and variation mechanisms. Their complementary operation provides a plausible explanation for the observed approximation behavior of the complete HV-ADEA framework.

5.5.2. Relationship to Earlier Hypervolume-Based Evolutionary Algorithms

Hypervolume-based selection is an established approach in evolutionary multi-objective optimization. SMS-EMOA combines non-dominated sorting with the removal of the solution with the smallest hypervolume contribution in the worst-ranked front [27]. HypE develops hypervolume-based fitness assignment for mating and environmental selection, including estimation techniques that reduce computational costs when many objectives are involved [33]. Earlier studies have reported favorable approximation results using these principles. Accordingly, improvements associated with hypervolume-based selection are not unique to HV-ADEA.

The design emphasis of the present framework is the integration of feasible archive management, feasible gain-guided direction adaptation, and variation operators tailored to UAV–UGV task allocation. Hypervolume contributes both to the retention of existing solutions and to feedback that influences subsequent search, while the specialized operators address the operational dependencies of the application.

Applying hypervolume contribution-based filtering to another evolutionary framework may also improve objective space coverage. The extent of that improvement depends on the candidates generated by the framework, its constraint-handling strategy, the archive capacity, and the characteristics of the problem. Results reported on other benchmarks do not establish whether such an application would reproduce the present MRTA results under identical conditions. The current experiments evaluate the selected complete algorithms and do not include variants obtained by adding the same filtering rule to each baseline.

5.5.3. Interpretation of the Experimental Evidence

The distribution shown in Figure 5 concerns a representative M1 run and provides a qualitative illustration of objective space coverage and proximity to the empirical reference front. It is consistent with the aggregate M1 results in Tables 5 and 6, where HV-ADEA obtains the highest mean HV and the lowest mean IGD. Nevertheless, its mean HV differs only slightly from that of NSGA-II, and the visual comparison does not independently establish statistical superiority.

Because HV-ADEA directly uses hypervolume during search, favorable HV outcomes are consistent with its selection criterion. IGD provides a complementary assessment of proximity to and coverage of the empirical reference set. The variation in performance across the test cases also indicates that the benefits of the framework depend on the instance characteristics.

The mechanism analysis above is a design-based interpretation of the existing observations. The experiments assess the integrated framework, and the individual contributions of archive filtering, direction adaptation, and specialized variation cannot be determined separately from the present complete-algorithm comparisons.

6. Conclusions

This paper investigated a centralized multi-objective task allocation problem for heterogeneous UAV–UGV teams in post-disaster emergency material distribution. The proposed formulation considers static, known demands, UGVs serving as mobile UAV bases, and split deliveries. It jointly models task allocation, routing, delivery quantities, and aerial–ground synchronization with three objectives: minimizing urgency-weighted demand completion time, minimizing operating cost, and minimizing maximum normalized workload. Accessibility, payload, inventory, energy, and synchronization constraints are incorporated to represent the operational dependencies between the two platforms.

To address the resulting constrained combinatorial optimization problem, we developed HV-ADEA, a hypervolume-guided adaptive decomposition evolutionary algorithm. The method combines decomposition-based search with an HV-controlled feasible nondominated archive. Feasible HV gains guide the adjustment of search directions, while a hybrid representation, synchronized decoding, and bounded iterative repair handle coupled allocation and scheduling decisions. Domain-specific operators explore changes to mobile base locations, UAV sorties, delivery quantities, and rendezvous bottlenecks.

Experiments on six test cases compared HV-ADEA with NSGA-II, CCMO, BiCo, EMCMO, and C3M. The HV and IGD trajectories reveal that its main strength lies in late-stage improvement on several medium- and large-scale cases. HV-ADEA achieves the highest final HV and lowest final IGD on M1. On L1 and L2, it obtains the second-highest final HV and the lowest final IGD, although some differences from the strongest competitors are small. Its performance on the small-scale cases is less competitive, and intermediate plateaus occur on several instances. These findings indicate that the method provides competitive final approximation sets under the evaluated settings while leaving room to improve early search efficiency.

Future work will investigate initialization and search budget allocation strategies to reduce prolonged plateaus, and use ablation studies to isolate the contributions of HV-guided direction adjustment and domain-specific operators. Broader evaluations with repeated runs and additional instance configurations will help establish the reliability and generality of the observed performance. Extending the formulation to uncertain demands, travel times, and robot availability is another path toward more realistic emergency response planning.

Author Contributions: Conceptualization, Y.Z. and C.W.; Methodology, Y.Z. and S.L.; Software, Y.Z.; Validation, S.L.; Formal analysis, Y.Z.; Investigation, Y.Z.; Writing, original draft preparation, Y.Z.; Writing, review and editing, S.L.; Visualization, Y.Z. and C.W.; Project administration, C.W. All authors have read and agreed to the published version of the manuscript.

Funding: This research was funded by a project funded by the Jiangsu Provincial Department of Science and Technology, grant number 26042501.

Institutional Review Board Statement: Not applicable.

Data Availability Statement: Data available on request from the authors.

Conflicts of Interest: The authors declare no conflicts of interest.

References

1. Erdelj, M.; Król, M.; Natalizio, E. Wireless sensor networks and multi-UAV systems for natural disaster management. *Comput. Netw.* **2017**, *124*, 72–86. [CrossRef]
2. Prakash, D.; Agrawal, A.; Khalid, S. Comparative analysis of UAVs: A study on payload capacity and performance. In *New Innovations in AI, Aviation, and Air Traffic Technology*; IGI Global Scientific Publishing: Hershey, PA, USA, 2024; pp. 128–149.
3. He, Y.; Hu, P.; Cao, Z.; Wang, K.; Ge, Z.; Qi, L.; Zeng, S.; Zheng, J.; Shi, J. Comparative endurance evaluation of hydrogen fuel cell and battery-electric propulsion systems for small commercial unmanned aerial vehicles. *J. Energy Storage* **2026**, *161*, 121813. [CrossRef]
4. Xiao, K.; Meng, Y.; Dai, X.; Zhang, H.; Quan, Q. A lifting wing fixed on multirotor UAVs for long flight ranges. In *Proceedings of the 2021 International Conference on Unmanned Aircraft Systems (ICUAS)*; IEEE: New York, NY, USA, 2021; pp. 1605–1610.
5. Bello, A.B.; Navarro, F.; Raposo, J.; Miranda, M.; Zazo, A.; Álvarez, M. Fixed-wing UAV flight operation under harsh weather conditions: A case study in Livingston island glaciers, Antarctica. *Drones* **2022**, *6*, 384. [CrossRef]
6. Chandran, I.; Vipin, K. Multi-UAV networks for disaster monitoring: Challenges and opportunities from a network perspective. *Drone Syst. Appl.* **2024**, *12*, 1–28. [CrossRef]
7. Gerkey, B.P.; Matarić, M.J. A formal analysis and taxonomy of task allocation in multi-robot systems. *Int. J. Robot. Res.* **2004**, *23*, 939–954. [CrossRef]
8. Nunes, E.; Manner, M.; Mitiche, H.; Gini, M. A taxonomy for task allocation problems with temporal and ordering constraints. *Robot. Auton. Syst.* **2017**, *90*, 55–70. [CrossRef]
9. Korsah, G.A.; Stentz, A.; Dias, M.B. A comprehensive taxonomy for multi-robot task allocation. *Int. J. Robot. Res.* **2013**, *32*, 1495–1512. [CrossRef]
10. Ghassemi, P.; Chowdhury, S. Multi-robot task allocation in disaster response: Addressing dynamic tasks with deadlines and robots with range and payload constraints. *Robot. Auton. Syst.* **2022**, *147*, 103905. [CrossRef]
11. Beck, Z.; Teacy, W.T.L.; Rogers, A.; Jennings, N.R. Collaborative online planning for automated victim search in disaster response. *Robot. Auton. Syst.* **2018**, *100*, 251–266. [CrossRef]
12. Wang, Y.; Li, J.; Yang, X.; Peng, Q. UAV–Ground Vehicle Collaborative Delivery in Emergency Response: A Review of Key Technologies and Future Trends. *Appl. Sci.* **2025**, *15*, 9803. [CrossRef]
13. Zhu, Y.; Wang, S. Cooperative aerial and ground vehicle trajectory planning for post-disaster communications: An attention-based learning approach. *Veh. Commun.* **2023**, *42*, 100624.1–100624.13. [CrossRef]
14. Shi, Y.; Zhang, K.; Zhang, J.; Chen, M.; Yang, J.; Guo, H. Dynamic truck-drone cooperative delivery of emergency supplies considering secondary disasters. *Transp. Res. Part E Logist. Transp. Rev.* **2026**, *206*, 104543. [CrossRef]
15. Aoki, N.; Ishigami, G. Autonomous tracking and landing of an unmanned aerial vehicle on a ground vehicle in rough terrain. *Adv. Robot.* **2023**, *37*, 344–355. [CrossRef]
16. Aziz, H.; Pal, A.; Pourmiri, A.; Ramezani, F.; Sims, B. Task allocation using a team of robots. *Curr. Robot. Rep.* **2022**, *3*, 227–238. [CrossRef]
17. Alirezazadeh, S.; Alexandre, L.A. A survey on task allocation and scheduling in robotic network systems. *IEEE Internet Things J.* **2024**, *12*, 1484–1508. [CrossRef]
18. Calvo, A.; Capitán, J. Heterogeneous multirobot task allocation for long-endurance missions in dynamic scenarios. *IEEE Trans. Robot.* **2025**, *41*, 6494–6513. [CrossRef]
19. Munasinghe, I.; Perera, A.; Deo, R.C. A Comprehensive Review of UAV-UGV Collaboration: Advancements and Challenges. *J. Sens. Actuator Netw.* **2024**, *13*, 81. [CrossRef]
20. Shahar, F.S. UGV-UAV Integration Advancements for Coordinated Missions: A Review. *J. Intell. Robot. Syst.* **2025**, *111*, 69. [CrossRef]

21. Chen, K.; Zhao, W.; Liu, Y.; Xia, Y.; Liang, W.; Wang, S. UAV-UGV Cooperative Trajectory Optimization and Task Allocation for Medical Rescue Tasks in Post-Disaster Environments. *J. Intell. Robot. Syst.* **2026**. [CrossRef]
22. Luo, X.; Liu, C. Simultaneous task allocation and planning for multi-robots under hierarchical temporal logic specifications. *IEEE Trans. Robot.* **2025**, *41*, 5040–5059. [CrossRef]
23. Liu, W.; Majcherczyk, N.; Pecora, F. Scalable Multi-Robot Task Allocation and Coordination under Signal Temporal Logic Specifications. In *Proceedings of the 2025 IEEE International Conference on Robotics and Automation (ICRA)*; IEEE: New York, NY, USA, 2025; pp. 3933–3939.
24. Altundas, B.; Chen, S.; Singh, S.; Deo, S.; Cho, M.; Gombolay, M. Heterogeneous Graph Transformers for Simultaneous Mobile Multi-Robot Task Allocation and Scheduling under Temporal Constraints. *Adv. Neural Inf. Process. Syst.* **2026**, *38*, 90611–90648.
25. Pan, S.; Cheng, A.; Sun, Y.; Kang, K.; Pais, C.; Zhou, Y.; Shen, Z.J.M. Using drone swarm to stop wildfire: A predict-then-optimize approach. *arXiv* **2024**, arXiv:2411.16144.
26. Wu, G.; Shu, T.; Shang, K.; Ishibuchi, H. Normalization in R2-Based Hypervolume and Hypervolume Contribution Approximation. In *Proceedings of the 2023 IEEE Symposium Series on Computational Intelligence (SSCI)*; IEEE: New York, NY, USA, 2023; pp. 449–456. [CrossRef]
27. Bader, J.; Zitzler, E. HypE: An Algorithm for Fast Hypervolume-Based Many-Objective Optimization. *Evol. Comput.* **2011**, *19*, 45–76. [CrossRef] [PubMed]
28. Deb, K.; Pratap, A.; Agarwal, S.; Meyarivan, T. A Fast and Elitist Multiobjective Genetic Algorithm: NSGA-II. *IEEE Trans. Evol. Comput.* **2002**, *6*, 182–197. [CrossRef]
29. Tian, Y.; Zhang, T.; Xiao, J.; Zhang, X.; Jin, Y. A Coevolutionary Framework for Constrained Multiobjective Optimization Problems. *IEEE Trans. Evol. Comput.* **2021**, *25*, 102–116. [CrossRef]
30. Liu, Z.; Wang, B.; Tang, K. Handling Constrained Multiobjective Optimization Problems via Bidirectional Coevolution. *IEEE Trans. Cybern.* **2022**, *52*, 10163–10176. [CrossRef] [PubMed]
31. Qiao, K.; Yu, K.; Qu, B.; Liang, J.; Song, H.; Yue, C. An Evolutionary Multitasking Optimization Framework for Constrained Multiobjective Optimization Problems. *IEEE Trans. Evol. Comput.* **2022**, *26*, 263–277. [CrossRef]
32. Sun, R.; Zou, J.; Liu, Y.; Yang, S.; Zheng, J. A Multistage Algorithm for Solving Multiobjective Optimization Problems With Multiconstraints. *IEEE Trans. Evol. Comput.* **2023**, *27*, 1207–1219. [CrossRef]
33. Beume, N.; Naujoks, B.; Emmerich, M. SMS-EMOA: Multiobjective selection based on dominated hypervolume. *Eur. J. Oper. Res.* **2007**, *181*, 1653–1669. [CrossRef]

Disclaimer/Publisher's Note: The statements, opinions and data contained in all publications are solely those of the individual author(s) and contributor(s) and not of MDPI and/or the editor(s). MDPI and/or the editor(s) disclaim responsibility for any injury to people or property resulting from any ideas, methods, instructions or products referred to in the content.